



Calhoun: The NPS Institutional Archive
DSpace Repository

Theses and Dissertations

1. Thesis and Dissertation Collection, all items

1959

Investigation of a two-dimensional low-speed cascade.

Eshman, John R.

Monterey, California: U.S. Naval Postgraduate School

<http://hdl.handle.net/10945/14359>

Downloaded from NPS Archive: Calhoun



Calhoun is the Naval Postgraduate School's public access digital repository for research materials and institutional publications created by the NPS community. Calhoun is named for Professor of Mathematics Guy K. Calhoun, NPS's first appointed -- and published -- scholarly author.

Dudley Knox Library / Naval Postgraduate School
411 Dyer Road / 1 University Circle
Monterey, California USA 93943

<http://www.nps.edu/library>

NPS ARCHIVE
1959
ESHMAN, J.

INVESTIGATION OF A TWO-DIMENSIONAL
LOW-SPEED CASCADE

JOHN R. ESHMAN

LIBRARY
U.S. NAVAL POSTGRADUATE SCHOOL
MONTEREY, CALIFORNIA

INVESTIGATION OF A
TWO-DIMENSIONAL LOW-SPEED CASCADE

* * * * *

John R. Eshman

NPS ARCHIVE

1959

ESHMAN, J.

~~Thesis~~

INVESTIGATION OF A
TWO-DIMENSIONAL LOW-SPEED CASCADE

by

John R. Eshman

This work is accepted as fulfilling
the thesis requirements for the degree of

MASTER OF SCIENCE

IN

MECHANICAL ENGINEERING

from the

United States Naval Postgraduate School

ABSTRACT

It is the purpose of this thesis to investigate a unique cascade test rig designed by the Department of Aeronautics, United States Naval Postgraduate School, where an inlet guide is arranged ahead of the cascade to be tested to simulate or approach the flow conditions that occur in actual machines. The cascade test rig is described and illustrated in section 2. Relations for the determination of the lift and drag coefficients are derived from the application of the momentum theorem. Results calculated from measured data are compared with the results published in the literature for geometrically similar cascades not equipped with an inlet guide vane assembly. Modifications to the present design are suggested.

ACKNOWLEDGMENT

The writer wishes to express his appreciation to Professor M. H. Vavra for the assistance and encouragement given him in this investigation.

TABLE OF CONTENTS

Section	Title	Page
1.	Introduction	1
2.	Description of the Cascade Test Rig	5
3.	Description of Measuring Devices	21
4.	Derivation of the Force Acting on a Test Vane	24
5.	Derivation of the Drag Coefficient of the Test Vanes	32
6.	Derivation of the Drag Coefficient from Thermodynamic Relationships	37
7.	Data Required for Determination of Cascade Performance	46
8.	Static Pressure Distribution in the Cascade	47
9.	Blade Loading Limit	69
10.	Results	71
11.	Conclusions	77
12.	Recommendations	78
	Bibliography	81
	Appendix Accuracy of Results	82

LIST OF ILLUSTRATIONS

Figure		Page
1.	Cross Section of a Typical Two-Dimensional Cascade Tunnel	2
2.	Schematic Diagram of Cascade Test Rig	6
3.	Diffuser	7
4.	General View of Cascade Test Rig from Right Hand Side	8
5.	General View of Cascade Test Rig from Left Hand Side	9
6.	Full Size Horizontal Cross Section of Cascade	11
7.	View of Cascade Showing Inlet Guide Vanes, Test Vane Holder and Sheet Brass Wall	12
8.	View of Cascade Showing Pressure Tap Slider and Angle Measuring Device	14
9.	View of Cascade Showing Wooden Upper and Lower Walls	15
10.	Full Size Horizontal Cross Section of Inlet Guide Vane Assembly	16
11.	View B-B of Inlet Guide Vane Assembly	17
12.	Section A-A of Inlet Guide Vane Assembly	18
13.	Guide Vane Profiles for 30, 55 and 65 Degrees	19
14.	Cross Section of Tip of Angle Measuring Probe	22
15.	Fluid Flow Through a "Control Surface"	24
16.	Flow of an Incompressible Fluid Through a Row of Stationary Vanes	27
17.	Illustration of the Angle ϕ	31
18.	Control Surface for the Application of the Momentum Theorem Between Stations 0 and 1	33

Figure		Page
19.	Illustration of the Velocities \bar{V}_0 , \bar{V}_3 and \bar{V}_s and the Resolution of the Force \bar{F} into Lift and Drag Components	35
20.	System for Calculating Energy Relations in Flow	37
21.	An Enthalpy-Entropy Diagram of the Fluid Through Cascade for Decelerated Flow	39
22.	Relationship of Velocity V and Angle of Fluid Flow α	46
23.	Initial Pressure Survey	48
24.	Screen Details	49
25.	Final Pressure Survey	50
26.	Static Pressure Profile	51
27.	Static Pressure Profile. Test Vanes Removed	53
28.	Static Pressure Profile. Upper Wall Contour Fixed. Lower Wall Contour Varied	54
29.	Lower Wall Contours	56
30.	Static Pressure Profile. Lower Wall Contour Fixed. Upper Wall Contour Varied	57
31.	Upper Wall Contours	58
32.	Initial Static Pressure Profile. Test Vanes Reinstalled	59
33.	Final Static Pressure Profile. Test Vanes Reinstalled	61
34.	Lower Wall Contours with Test Vanes Reinstalled	62
35.	Total Pressure Ahead of Test Vanes	63
36.	Static Pressure Ahead of Test Vanes	64
37.	Angle of Fluid Flow Ahead of the Test Vanes	65
38.	Total Pressure After Test Vanes	66

Figure		Page
39.	Static Pressure After Test Vanes	67
40.	Angle of Fluid Flow After Test Vanes	68
41.	Upper and Lower Wall Modification	79

Table		Page
I	Comparison of Approximate and Exact Values of P_{s1}/P_s	45
II	Results Calculated From Test Data	72
III	Comparison of Results	74
IV	Representative Values of P_o and α	86

TABLE OF SYMBOLS

C_D	drag coefficient, dimensionless
C_L	lift coefficient, dimensionless
D	drag force, pounds
\overline{F}	force exerted by fluid on test vane, pounds
F_a	axial component of force exerted by fluid on test vanes, pounds
F_u	tangential component of force exerted by fluid on test vanes, pounds
\overline{G}	gravitational force, pounds
L	lift force, pounds
M	Mach number, V/a , dimensionless
N_R	Reynolds number, $\frac{\rho V c}{\mu}$, dimensionless
R	volume bounded by control surface S , feet cubed
R_g	gas constant of the fluid
S	area of control surface, feet squared
T	temperature, degrees Rankine
\overline{V}	velocity of fluid, feet per second
V_a	axial component of velocity, feet per second
V_u	tangential component of velocity, feet per second
a	speed of sound, feet per second
c	chord of test vanes, feet
c_p	specific heat at constant pressure, British Thermal Units per pound-degree Rankine
c_v	Specific heat at constant volume, British Thermal Units per pound-degree Rankine
dm_s	mass flow rate through an element of area, slugs per second
dS	element of surface area, feet squared

h	test vane height, feet
h	enthalpy, British Thermal Units per pound
\bar{i}	unit vector in the axial direction
\bar{j}	unit vector in the tangential direction
m_s	mass flow rate, slugs per second
\bar{n}	unit vector normal to the surface
p	static pressure, pounds per foot squared
p_0	dynamic pressure, pounds per foot squared
p_s	total pressure, pounds per foot squared
q	heat exchanged between a system and its surroundings, British Thermal Units per pound
s	test vane spacing, feet
\bar{t}	unit vector, parallel to S , orthogonal to \bar{n} , in direction of shear stress
t	mean effective thickness of test vanes, feet
x	variable of integration over vane spacing s
α	measured angle between fluid flow and horizontal, degrees
α_a	angle of attack of test vanes, degrees
β	angle between \bar{V} and horizontal, degrees
$\Delta\beta$	turning angle, $\beta_2 - \beta_3$, degrees
γ	ratio of specific heats c_p/c_v , dimensionless
η	blading efficiency, dimensionless
λ	a multiple, not necessarily an integer, of vane spacing s , dimensionless
ϕ	angle between \bar{F} and vertical, degrees
ρ	density, slugs per foot cubed
σ	solidity of cascade c/s , dimensionless

τ	shear stress, pound per foot squared
ξ	loss coefficient, $\frac{1}{\eta} - 1$, dimensionless
ζ	loss coefficient, $(1 - \eta)$, dimensionless

Subscripts:

P	profile of test vane
S	stagnation, or reservoir, value
a	axial direction
av	average value
p	static pressure
th	theoretical
u	tangential direction
τ	shear stress
0	station 0
1	station 1
2	station 2
3	station 3
∞	station ∞ , the average of conditions at stations 0 and 3

Vector quantities are denoted by bars over letters.

1. Introduction.

For the design of axial-flow turbo-machinery it is necessary to know the three-dimensional viscous compressible flow of high velocity through successive rows of stationary and moving blades. No complete analytical solution has yet been provided for this problem. Those areas of the problem for which analytical solutions are available, however, are based on an idealized fluid flow which does not consider the effects of one or more of the following physical realities: compressibility, finite blade spacing and viscosity.¹ As a result, experimental data must be used to supplement the idealized theoretical solutions.²

Experimental data may be obtained directly from the test of rotating turbo-machinery. Another source of experimental information is the result of stationary cascade tests. One type of stationary cascade, a rectilinear cascade, is obtained by intersecting a row of blades of an axial flow turbo-machine with a cylinder and developing the cylinder into a plane. Air is blown through the rectilinear cascade in the direction of flow in the turbo-machine and then discharged into the atmosphere. Results of cascade tests of interest to

¹F. R. Fahland and L. L. Hawkins, An Electrical Analogy for Analysis of Flow Through Cascades, Thesis, U. S. Naval Postgraduate School, Monterey, California, 1958.

²L. J. Herrig, J. C. Emery and J. R. Erwin, Systematic Two-Dimensional Cascade Tests of NACA 65-Series Compressor Blades at Low Speeds, NACA TN 3916, February, 1957.

the designer include lift and drag coefficients, the pressure distribution about the surface of the blade, boundary layer behavior and turning angle.

The cross section of a typical cascade tunnel is shown in Fig. 1. One of the major difficulties encountered in this type of cascade is the control of the boundary layers ahead of the cascade. Figure 1 shows that the fluid passing along the lower contour of the channel must travel a greater distance before reaching the blades than the fluid flow passing along the upper wall. As the size of the boundary layer increases with the distance traveled along a wall, the thickness of the boundary layer at the lower wall is greater than that at the upper wall.

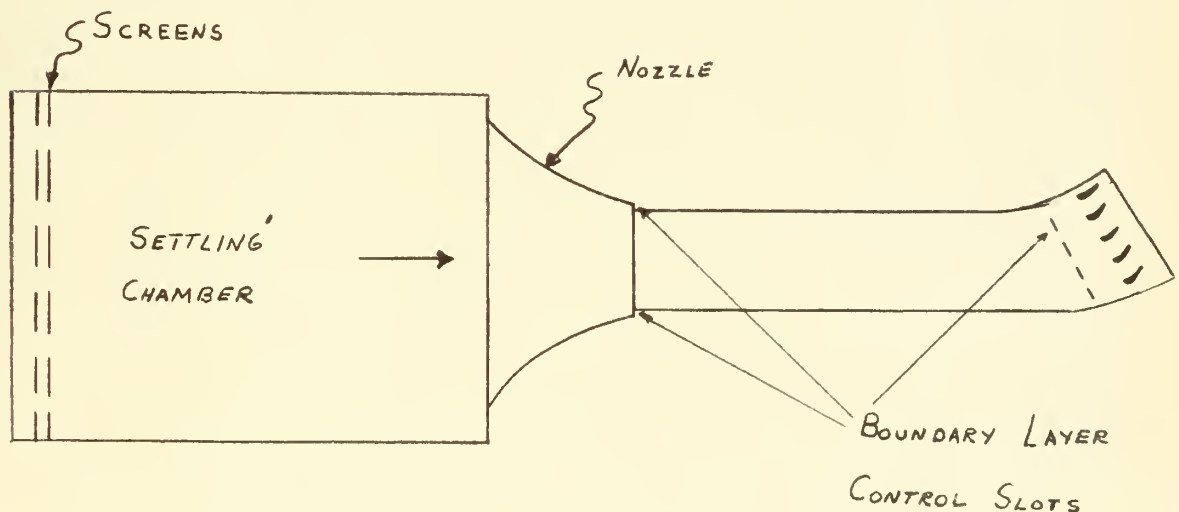


Figure 1. Cross Section of a Typical Two-Dimensional Cascade Tunnel.

The boundary layer problem is partially solved by the installation of boundary layer removal slots at the nozzle

discharge. To facilitate the removal of the boundary layers these slots are usually connected by piping to a source of vacuum. Still to be considered is the control of the boundary layer downstream of the nozzle. One method of control is the use of slots located in the walls of the cascade. A more effective method of boundary layer control is used by Herrig, Emery and Erwin in NACA TN 3916 [1]. Here the upper, lower and side walls of the cascade were constructed of a porous material and were encased in a sheet metal housing connected by piping to a vacuum system. Control of the boundary layer was effected by drawing off a portion of the fluid flow through the porous walls into the vacuum system.

All these cascade, however, idealize the fluid flow in that conditions of static and total pressure, velocity of fluid flow and flow angle are constant at the entrance of the cascade. Thus the effect of inlet guide vanes or preceding rows of blades, as encountered in turbo-machinery, is not considered. Recognizing this, a novel two-dimensional low-speed cascade was designed by the Department of Aeronautics, United States Naval Postgraduate School, Monterey, California. The uniqueness of this design lies in the incorporation of an inlet guide vane section at the entrance to the cascade. This cascade test rig, discussed in detail in the next section, has an advantage over conventional cascade wind tunnels in that boundary layer control devices are not required. This is the result of eliminating the dissimilarity in boundary layer thicknesses at the upper and lower walls

by using vertical cascading of the test vanes and the use of parallel side walls.

It is the objective of this thesis to:

A. Investigate the unique two-dimensional low-speed cascade designed by the Department of Aeronautics, United States Naval Postgraduate School, Monterey, California, by determining:

1. Conditions of pressure, fluid velocity and flow angle after the inlet guide vanes.

2. Conditions of pressure, fluid velocity and flow angle after the test vanes.

3. Lift and drag coefficients.

B. Evaluate the above characteristics by comparison with previously published results for geometrically similar cascades.

2. Description of the Cascade Test Rig.

The basic components of the cascade test rig, shown schematically in Fig. 2, are the prime mover, fan, diffuser, settling chamber, nozzle block and cascade. The prime mover employed was a Wagner Electric Company five horsepower, three phase, 440 volt a.c. motor. The fan used was a Hishock Shipboard Fan manufactured by the Buffalo Forge Company. The settling chamber, dimensions $22\frac{1}{2} \times 22\frac{1}{2} \times 34$ inches, was constructed of plywood. The diffuser, located between the fan discharge and the settling chamber inlet, is shown in Fig. 3. An interesting design feature of the cascade test rig was the length of the diffuser. In contrast to the diffusers used in conventional cascade tunnels, the one used in the present cascade test rig was of relatively short length. With a ratio of outlet area to inlet area of 1.6, separation of the flow would normally occur at the diffuser outlet, resulting in an uneven distribution of the flow at the discharge. By the use of screens placed between the fan and the settling chamber inlet the fluid flow can however be made to follow the shape of the diffuser walls with corresponding good conversion of the kinetic energy into static pressure.

The nozzle block was constructed of laminations of wood. The discharge section of the nozzle block was in the shape of a rectangle measuring eight inches in height and one and one-quarter inches in width. Photographs of the cascade test rig are shown in Fig. 4 and Fig. 5.

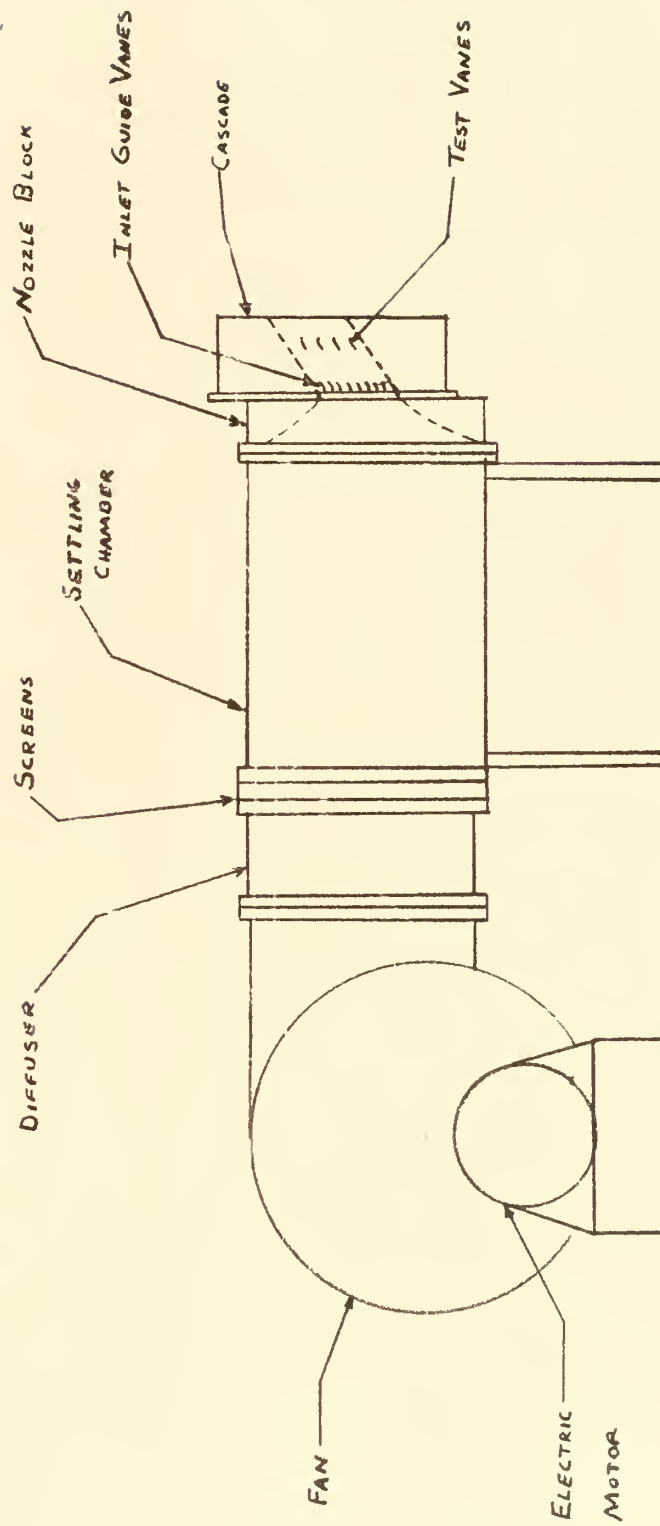


FIGURE 2. SCHEMATIC DIAGRAM OF CASCADE TEST RIG.

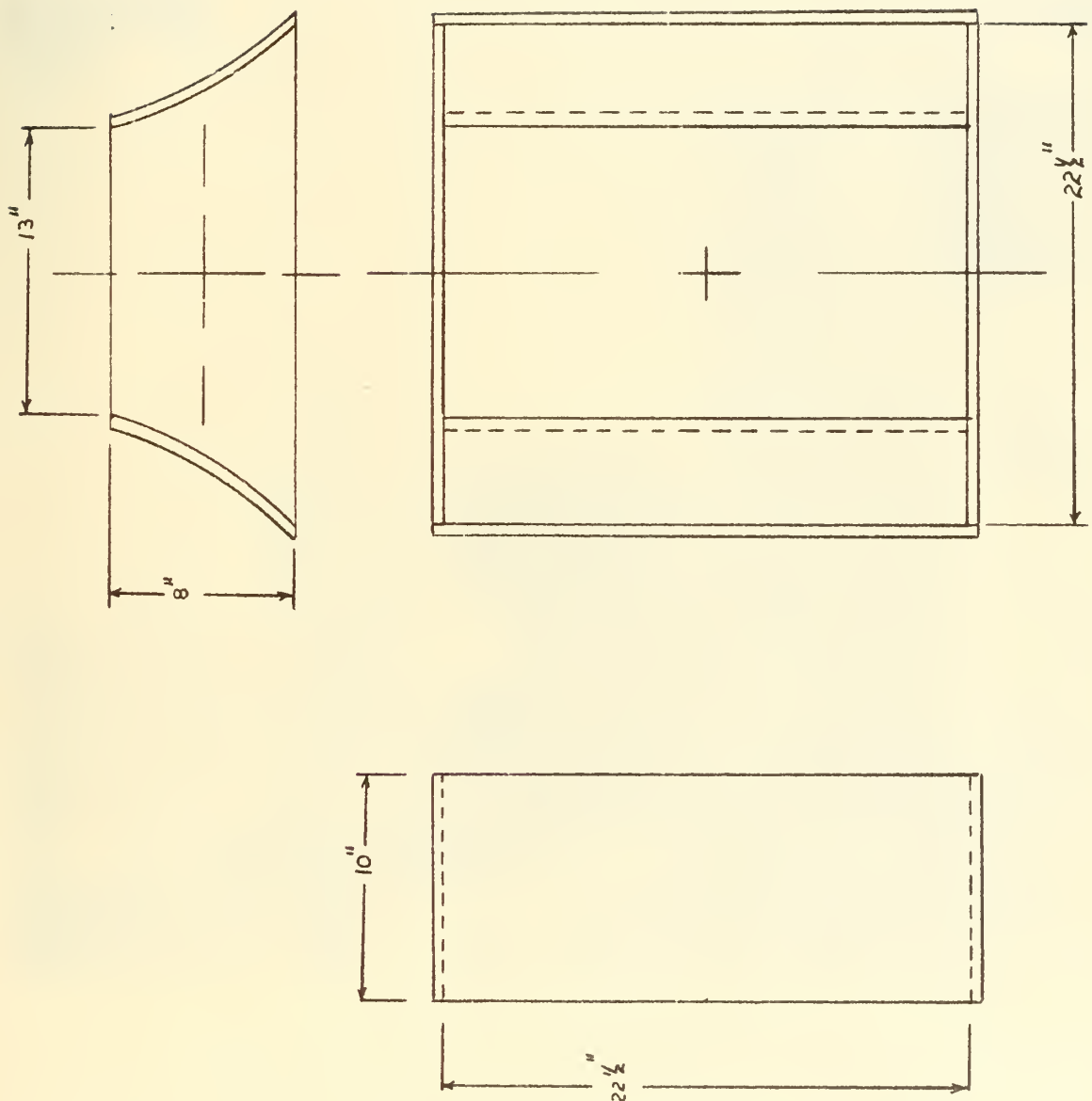


FIGURE 3. DIFFUSER

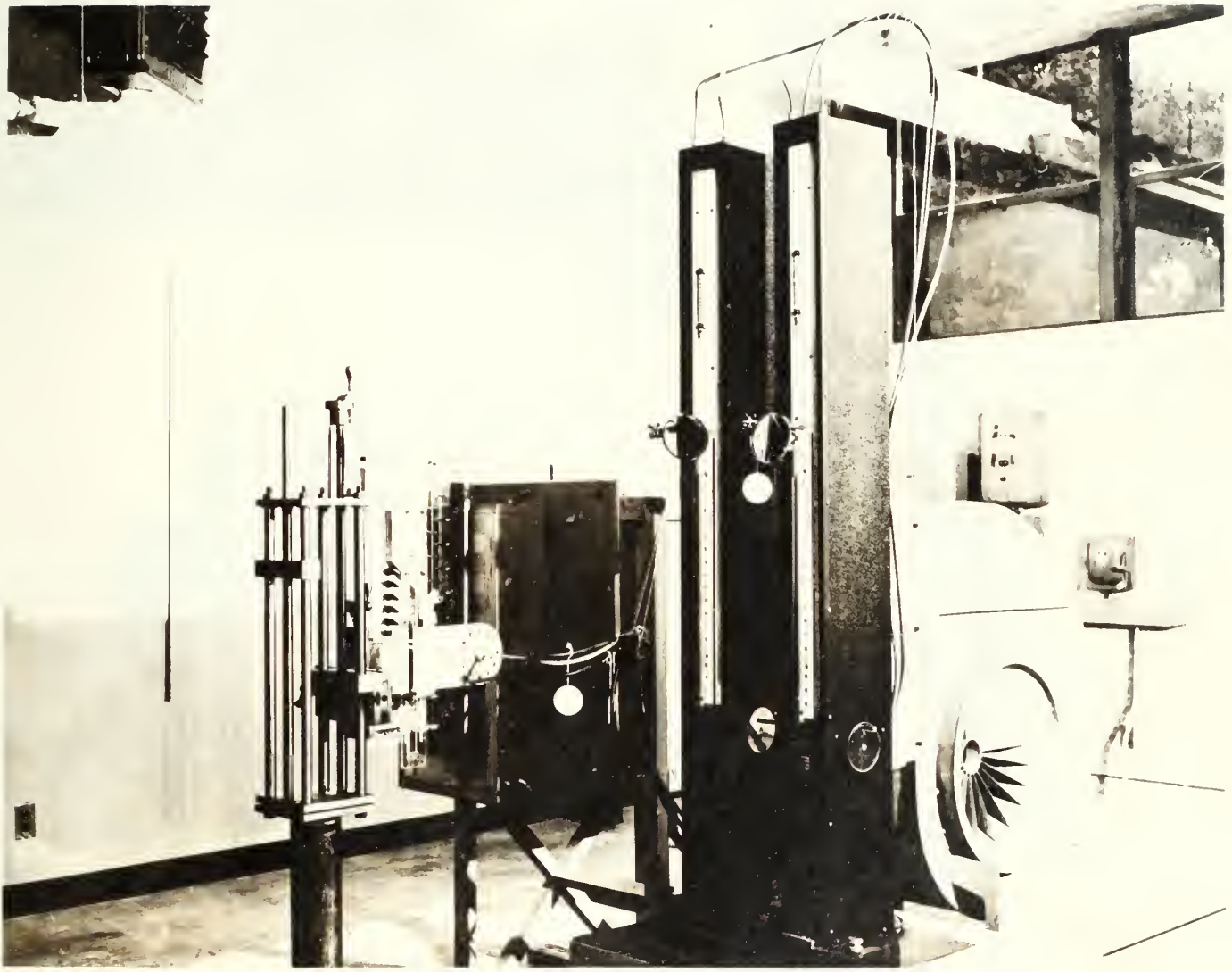


FIGURE 4 - GENERAL VIEW OF CASCADE TEST RIG FROM RIGHT HAND SIDE.

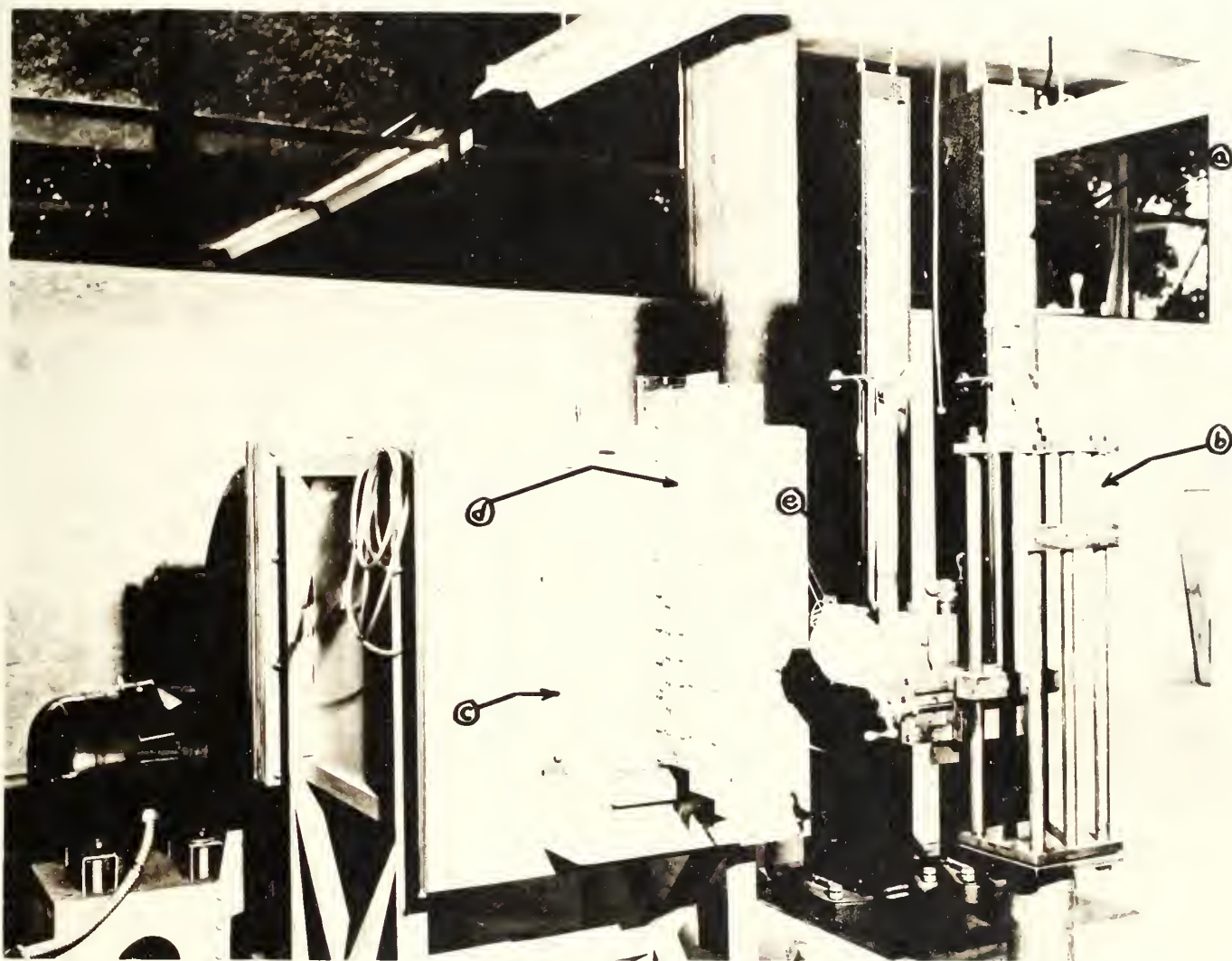


FIGURE 5 - GENERAL VIEW OF CASCADE TEST RIG FROM LEFT HAND SIDE SHOWING :
 (a) MICROMANOMETER, (b) LEAD SCREW DEVICE, (c) NOZZLE BLOCK,
 (d) CASCADE, (e) ANGLE MEASURING DEVICE.

Figure 6 shows a horizontal cross section of the cascade. The tunnel base, covers and pressure tap slider were constructed of clear plastic. Located between the inlet guide vane assembly and the test vane assembly, the pressure tap slider was drilled to permit entry of pitot-static tubes and angle measuring probes into the fluid flow. Movement of the pressure tap slider in the vertical direction was made possible by the use of several long narrow slots machined in that portion of the pressure tap slider which overlapped the cover. Brass studs were fitted through these slots into holes drilled and tapped in the cover. Nuts were used to apply a clamping force which held the pressure tap slider against the cover.

The test vane assembly was also constructed to permit vertical movement of the assembly upon the release of a clamping force applied by the method previously described. The vertical movement of the test vane assembly allowed positioning of the vanes as a group with respect to the upper or lower wall of the cascade. In addition, the test vanes were individually mounted to permit axial positioning for various angles of incidence. Figure 7 shows this construction.

Originally, the upper and lower walls of the cascade were constructed of thin sheet brass which permitted some degree of freedom in forming the contour of the upper and lower walls. The desired wall shape was obtained by securing the sheet brass side walls to pieces of masonite shaped in the desired configuration. Due to the difficulty in obtaining

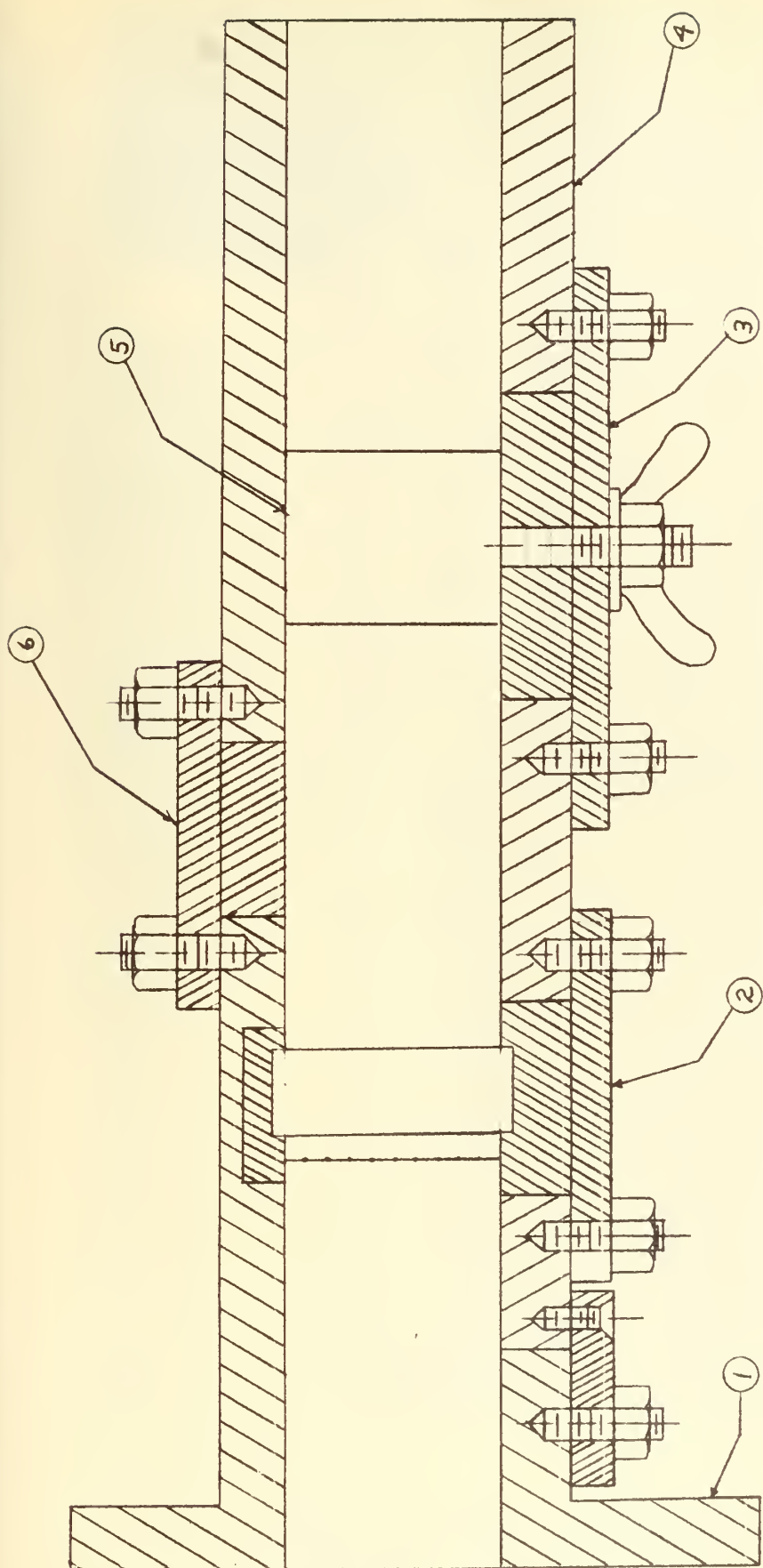


Figure 6. Full Size Horizontal Cross Section of Cascade Showing: 1- Tunnel Base; 2- Inlet Guide Vane Assembly; 3- Test Vane Assembly; 4- Cover; 5- Test Vane; 6- Pressure Tap Slider Assembly.

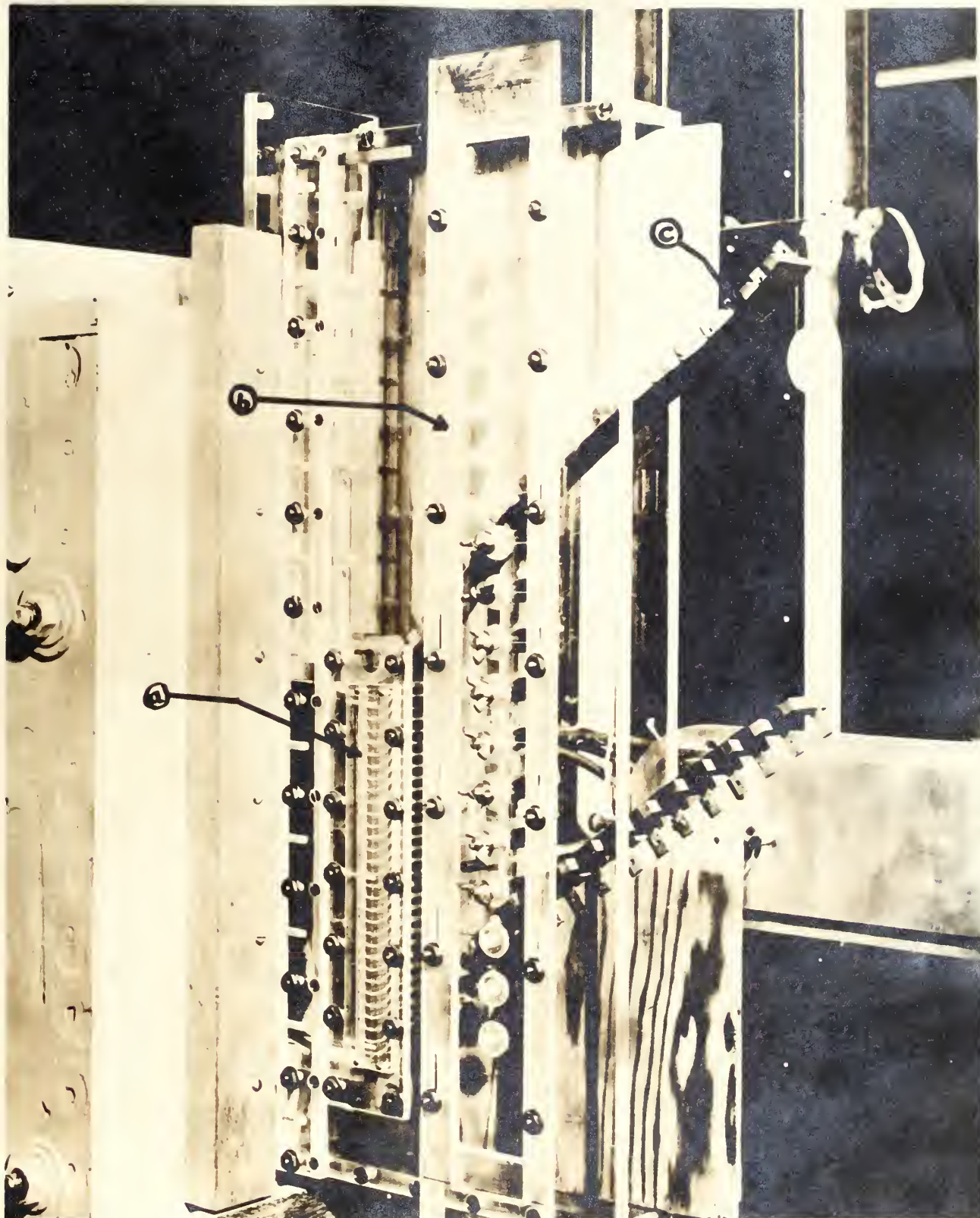


FIGURE 7 - VIEW OF CASCADE SHOWING : @ INLET GUIDE VANES ,
⑥ TEST VANE HOLDER , ③ SHEET BRASS WALL.

the proper static pressure profile downstream of the inlet guide vanes, this method of upper and lower side wall construction was rejected in favor of walls formed from solid blocks of wood. Figure 7 and Fig. 8 illustrate the use of sheet brass for upper and lower walls. Solid wooden walls are shown in Fig. 9.

The inlet guide vane assembly is shown in horizontal cross section in Fig. 10. Plastic was used in the construction of all parts of the assembly with the exception of the guide vanes and the turbulence screen. Figure 11 is view B-B of the horizontal cross section of the inlet guide vane assembly. In this view the zero degree guide vanes and only a portion of the turbulence screen were shown to preserve clarity. Section A-A of the horizontal cross section of the inlet guide vane assembly is shown in Fig. 12. In this view the guide vanes have been shaded in an attempt to make them distinguishable from the slots in the upper guide vane cover. The zero degree guide vanes are shown in this figure. Figure 13 illustrates the guide vane profiles for 30, 55 and 65 degree approach angles of the flow ahead of the test vanes. The 55 degree guide vane profile was used in this investigation.

The inlet guide vanes can be fabricated quite easily for any flow angle change desired through the inlet guide vane assembly. However, corresponding upper and lower guide vane covers must be machined. In addition, the configuration of the upper and lower walls is different for

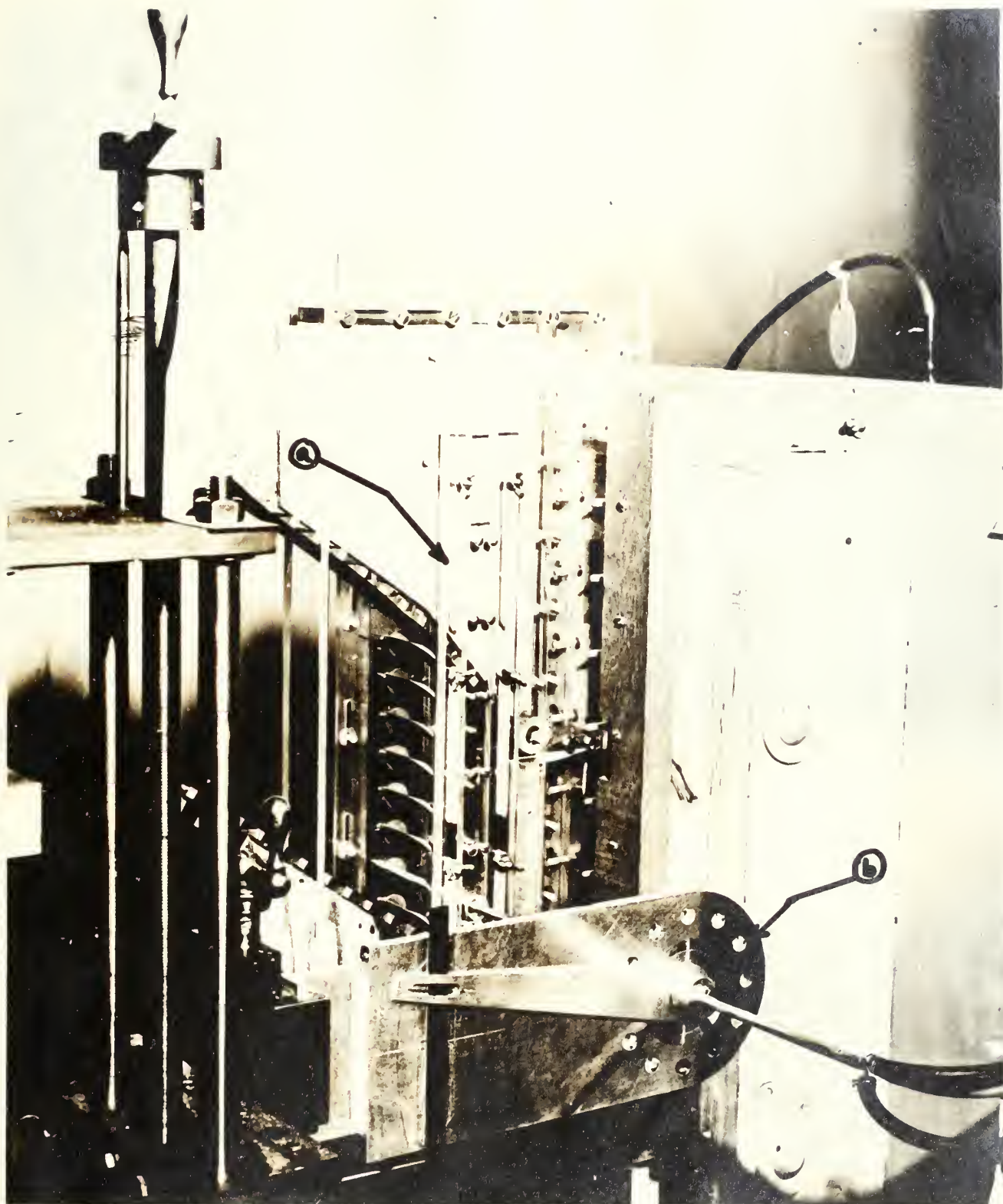


FIGURE 8 - VIEW OF CASCADE SHOWING: (A) PRESSURE TAP SLIDER,
(B) ANGLE MEASURING DEVICE.

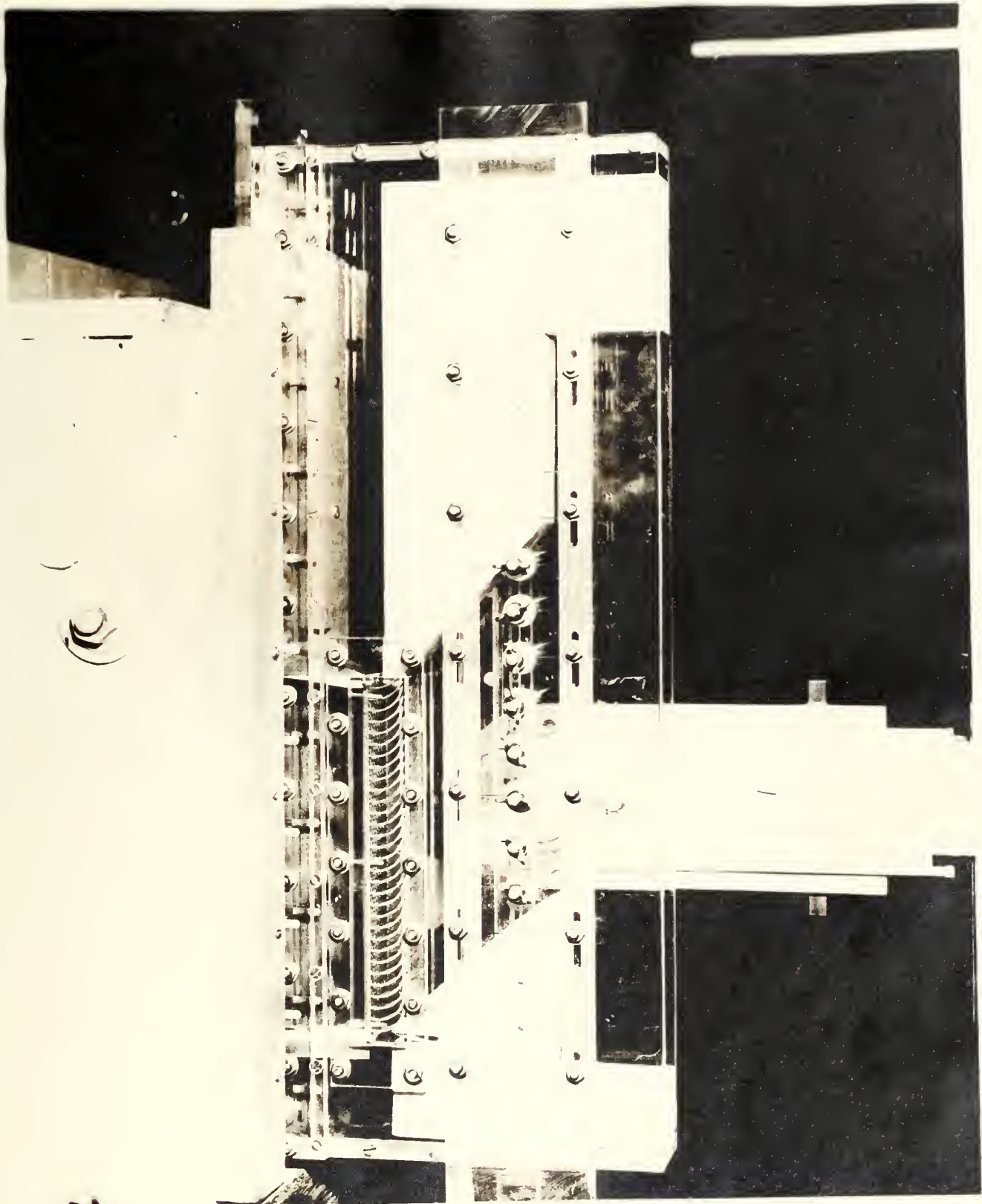


FIGURE 9 - VIEW OF CASCADE SHOWING WOODEN UPPER AND LOWER WALLS

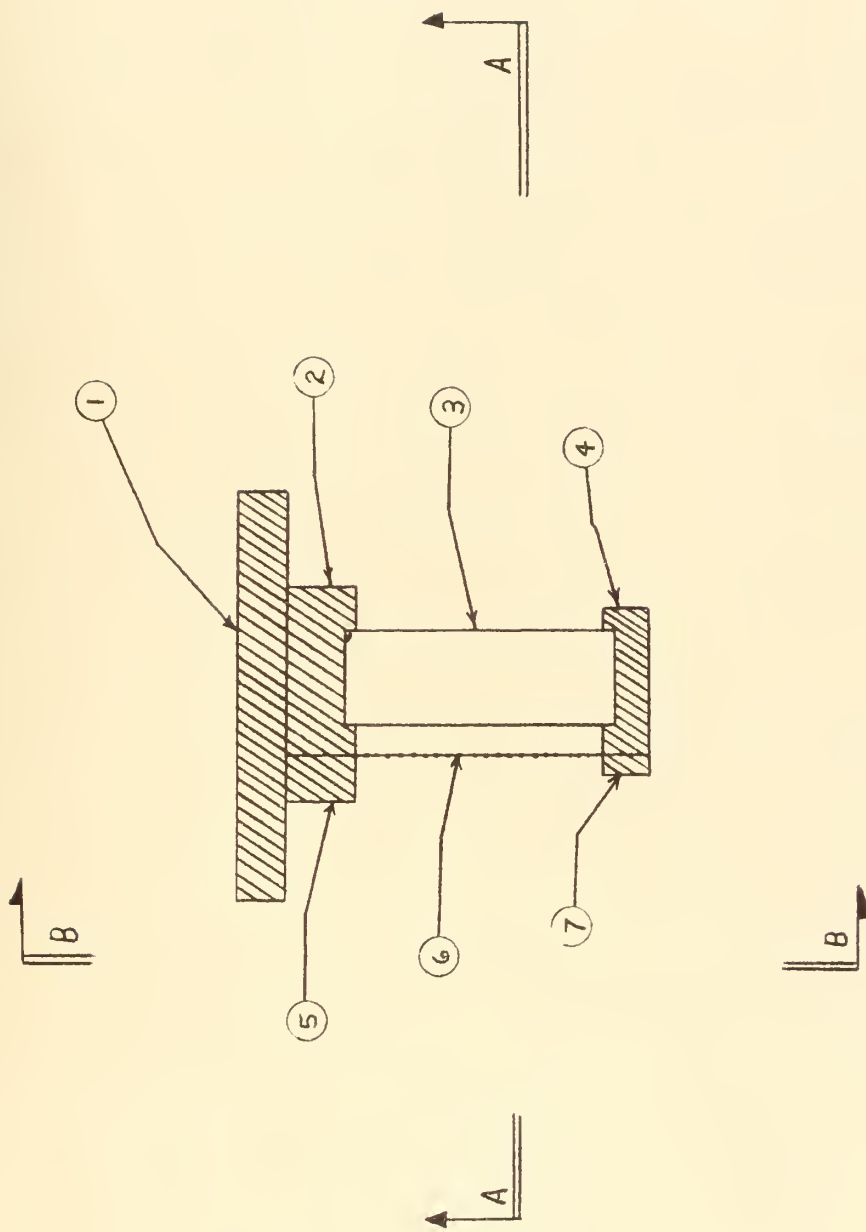


Figure 10. Full Size Horizontal Cross Section of Inlet Guide Vane Assembly Showing:
 1- Cover Plate; 2- Upper Guide Vane Cover; 3- Guide Vane; 4- Lower Guide Vane Cover;
 5- Upper Turbulence Screen Holder; 6- Turbulence Screen; 7- Lower Turbulence Screen Holder;
 Section A-A and View B-B.

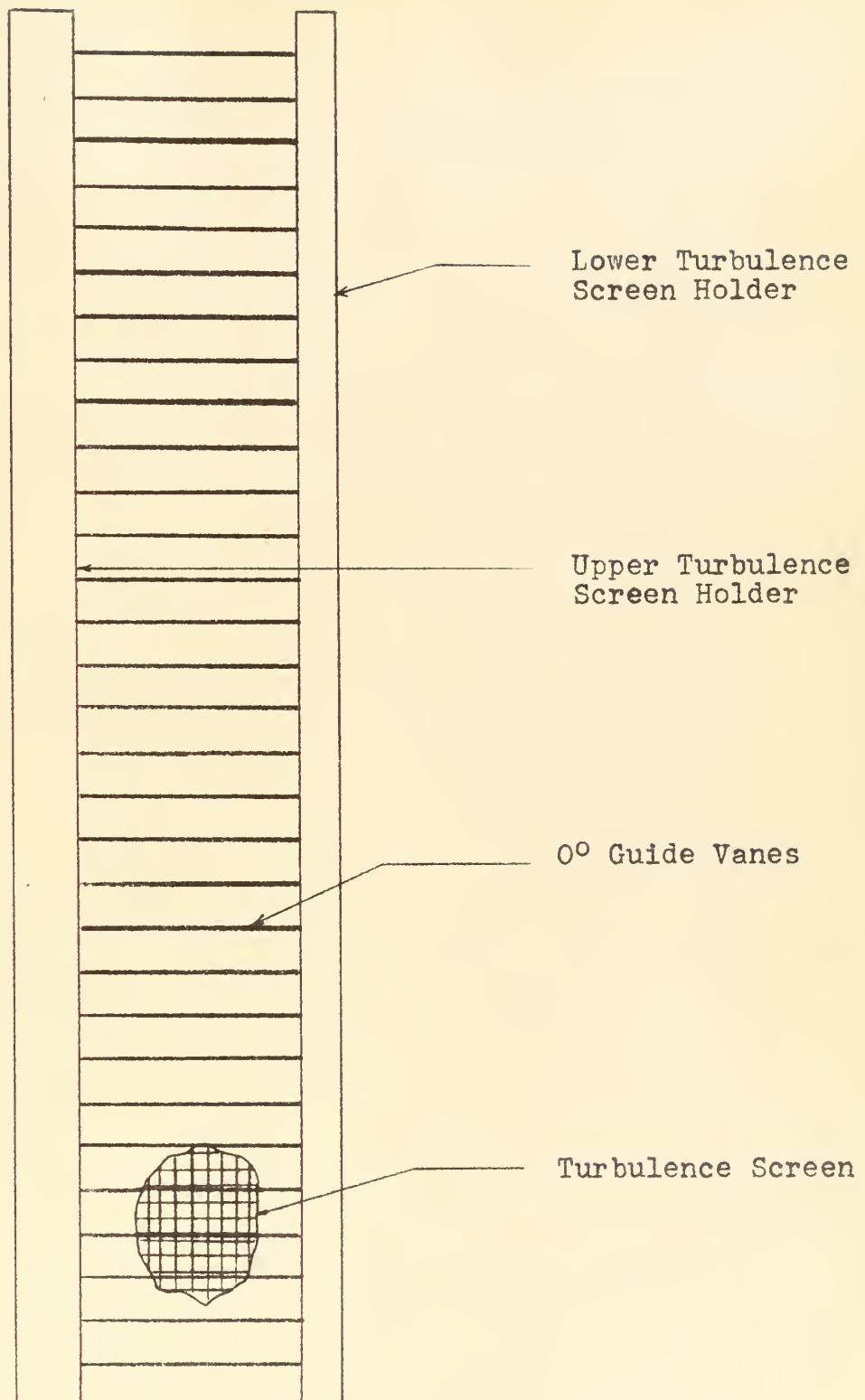


Figure 11. View B-B, Full Size, of Inlet Guide Vane Assembly.
Cover Plate Not Shown.

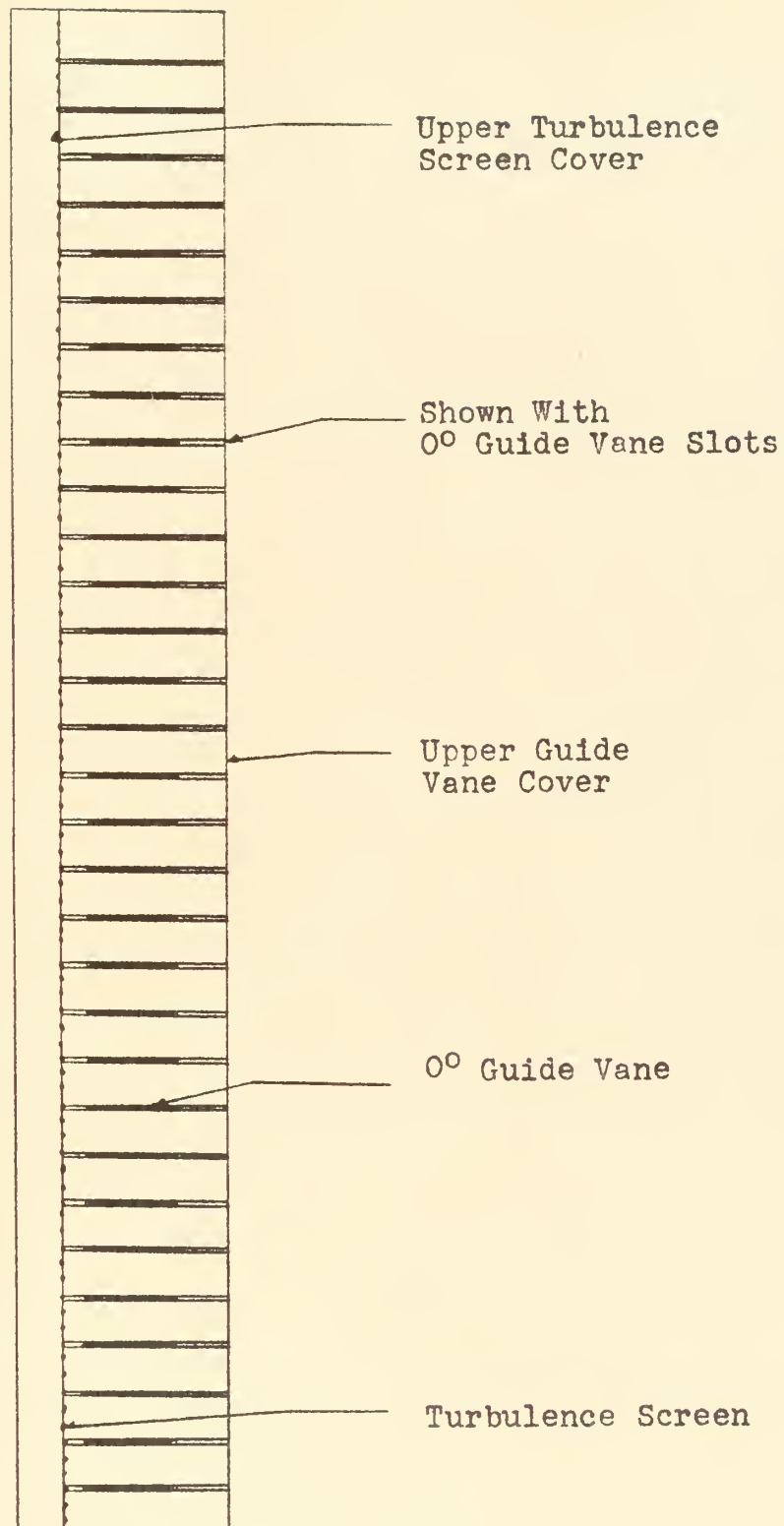


Figure 12. Section A-A, Full Size, Of Inlet Guide Vane Assembly, Cover Plate Not Shown.

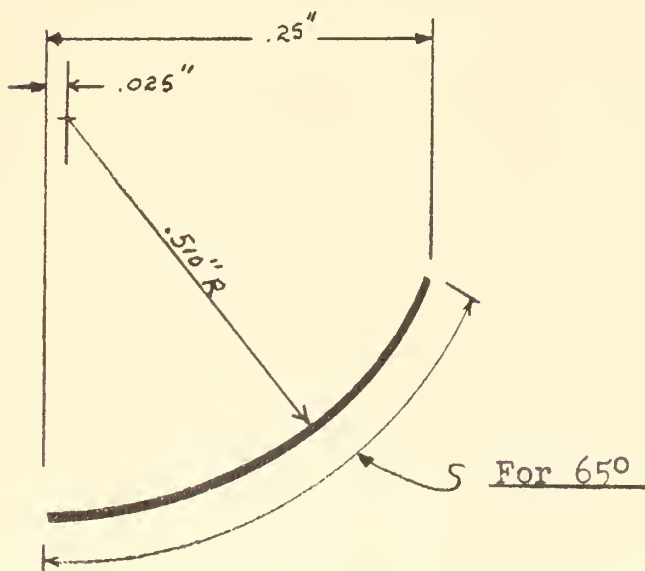
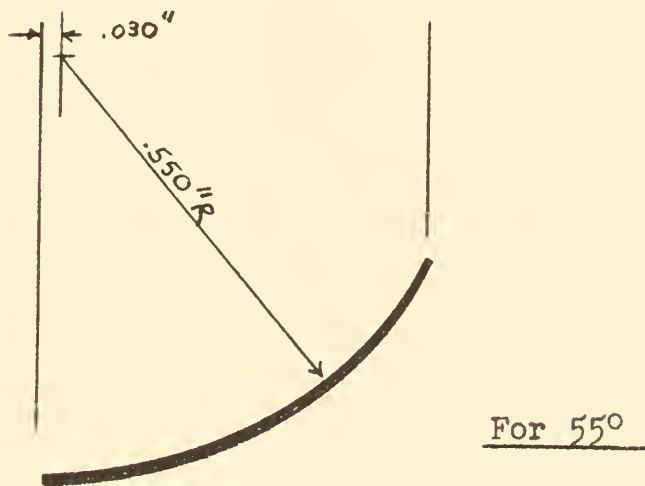
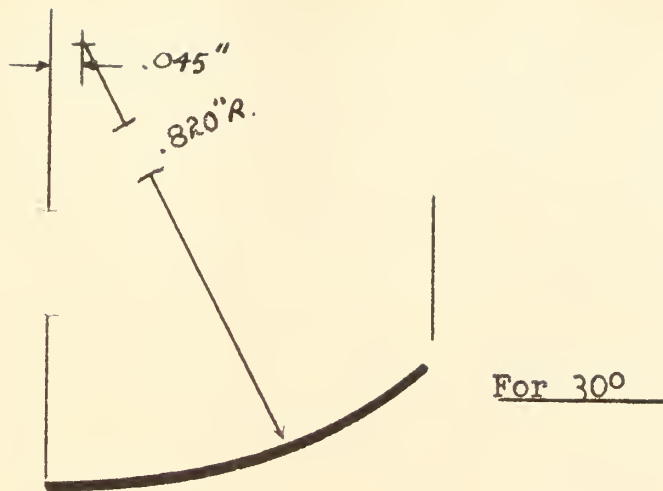


Figure 13. Guide Vane Profiles For 30°, 55°, 65° .

each flow angle. This requires that appropriate masonite or wooden contours must be provided for each set of inlet guide vanes.

3. Description of Measuring Devices.

The lead screw device, shown in the foreground of Fig. 4 and Fig. 5, served as a support for the angle measuring device and controlled the movement of the pressure tap slider.

With the angle measuring device the angle between the fluid flow in the cascade and the horizontal direction was determined. This device consisted of a pointer attached to an angle measuring probe. The tip of the angle measuring probe is shown in cross section in Fig. 14. Three holes drilled from the outer surface of the tube connected to piping brought in from the opposite end of the probe. The middle hole was used to measure the total pressure of the fluid flow in the cascade. Pressure leads from the two symmetrically located holes were placed across a differential manometer. As can be seen from Fig. 14, if the middle hole is not lined up in the direction of the flow the pressure measured by the symmetrically located holes will not be equal, hence, there will be an unbalance in the differential manometer. The flow angle can be measured by turning the probe until this unbalance is removed, and the pressure measured by the middle hole then corresponds to the total pressure of the flow.

The flow angle at a particular probe position was determined by reading the vertical distance on the machinists rule as indicated by the cross hairs on the pointer. As the distance from the axis of the angle measuring probe to the pointer cross hairs was known, the angle was readily determined by trigonometric relations. Reference to Fig. 8 shows

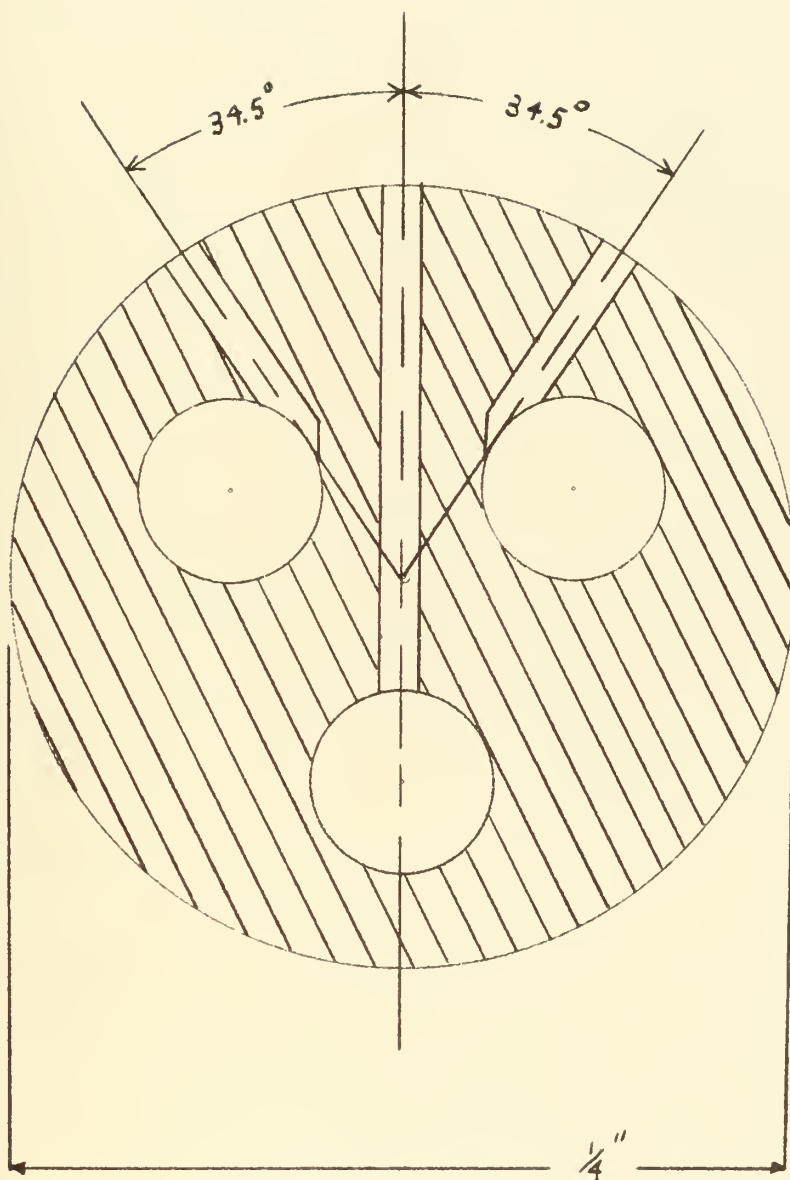


Figure 14. Cross Section Of Tip Of Angle Measuring Probe.
16 Times Full Size.

12 holes drilled thirty degrees apart on the scale arm of the angle measuring device. These holes were drilled to permit an initial angle, some multiple of 30 degrees, to be preset into the angle measuring device. This construction had two advantages: it permitted the measurement of widely different fluid flow angle, and it reduced the magnitude of the angle to be measured by the machinists rule-pointer arm method to an angle of less than 15 degrees.

4. Derivation of the Force Acting on a Test Vane.

For purposes of analysis the flux of matter through a "control surface" is observed. The surface may be of arbitrary shape but area S must be completely filled with fluid. The volume, or region, enclosed by the surface S is denoted by R . Fluid flow enters the region R through surface S_1 at station 1 and leaves the region R through surface S_2 at station 2. At no other station does the fluid flow cross the surface S . Figure 15 shows such a flow field.

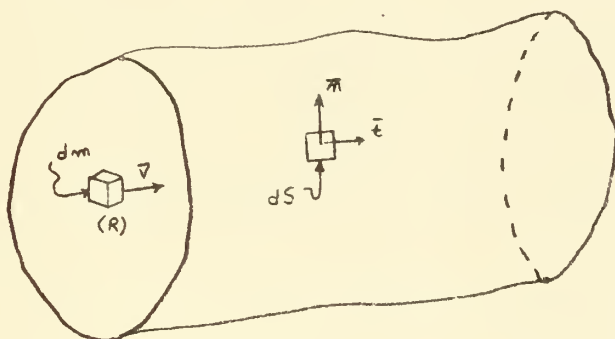


Figure 15. Fluid Flow Through a "Control Surface."
Surface Area is S , Volume of Region is R .

The momentum theorem can be stated for the flow in the following manner: The net force acting upon the bounding surface S of a fluid enclosing a region R is equal to the transport of momentum out of the region R minus the transport of momentum into the region R , plus any change in momentum due

to non-steady flow conditions within the region R, where these quantities must be added vectorially.

The forces acting on the fluid are of two types, surface forces and volume forces. Surface forces are caused by the presence of some type of medium adjacent to the surface S which encloses the region R. In viscous flow there can be a static pressure p acting normal to the surface S and a shear stress τ acting parallel to the surface S. Volume forces are due solely to gravity effects, if electric and magnetic forces are ignored. We will represent the gravity force by the vector \vec{G} .

Considering the fluid flow shown in Fig. 15, the momentum theorem may be used to write the following vector equation between the inlet at station 1 and the outlet at station 2.

$$\frac{\partial}{\partial t} \left[\int_R d_m \vec{V} \right] + \int_{S_2} d_{m_{S_2}} \vec{V}_2 - \int_{S_1} d_{m_{S_1}} \vec{V}_1 = \int_S \vec{n} p dS + \int_S \vec{e} \tau dS + \vec{G} \quad (1)$$

An element of surface area is denoted by $\vec{n} dS$, where \vec{n} is a unit vector normal to the surface S that points away from the region R. The velocity which transports matter through the element of area $\vec{n} dS$, is \vec{V} , so that the rate of flow of matter d_{m_S} through dS is

$$d_{m_S} = \vec{n} \cdot \vec{V} \rho dS \quad (2)$$

The normal pressure is directed inward, so that, if \vec{n} is the outward normal to the surface, the force acting on an element of area, is given by $-\vec{n} p dS$. The total force acting

on the fluid in the region R due to the pressure p is

$$\bar{F}_p = \int_s -\bar{n} p dS \quad (3)$$

The shear stress τ acting on the surface S is opposing the flow of the fluid through R . Therefore, if \bar{t} is the unit vector parallel to the surface S and orthogonal to \bar{n} , the force on an element of area $\bar{t} dS$ is given by $-\bar{t} \tau dS$. The total force acting on the fluid in the region R due to the shear stress τ is

$$\bar{F}_\tau = \int_s -\bar{t} \tau dS \quad (4)$$

Having applied the momentum theorem for a completely general case, it will now be applied to the fluid flow through a cascade of test vanes. The basic difference in the application of the momentum theorem in the two cases will be the existence of forces exerted on the fluid flow by the test vanes of the cascade. By using the momentum theorem an equation containing these forces can be written. This equation may be rearranged to permit solving for the force of the profile on the fluid flow. In practice, the equal and opposite reaction, the force of the fluid flow on the profile, is of interest. This fact will be taken into consideration in the succeeding derivation.

Figure 16 shall refer to a flow of an incompressible fluid through a row of stationary vanes. The constant density of the fluid is ρ slugs/ft.³ The vane spacing in the direction of the row is W feet. The chord of the vanes is

c feet. The so-called solidity of the cascade σ is the ratio c/d .

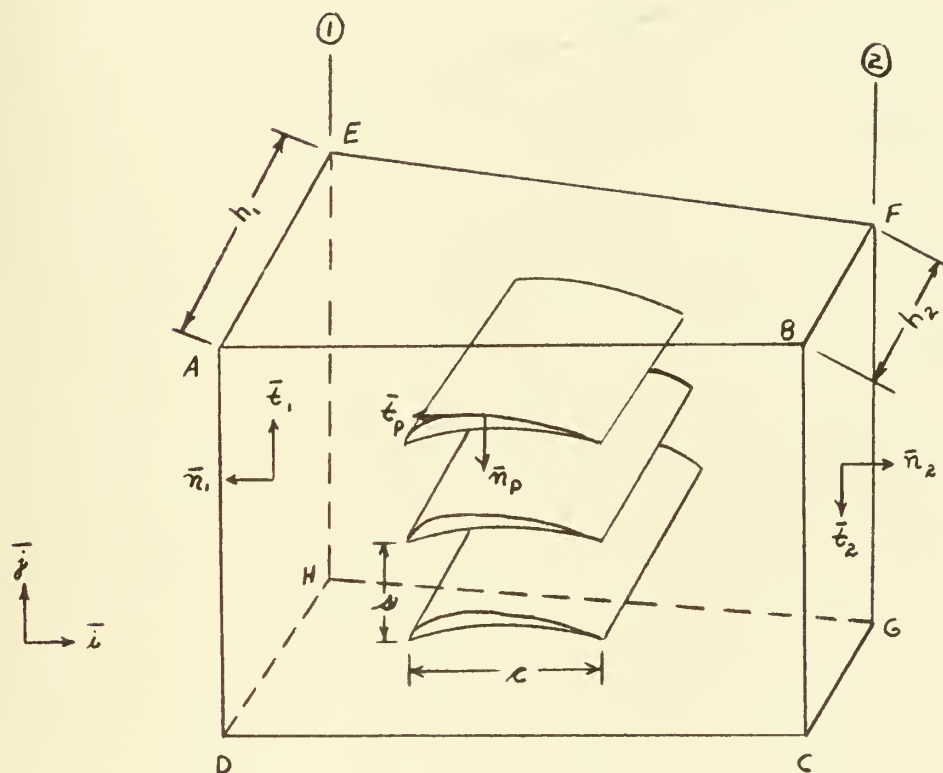


Figure 16. Flow of an Incompressible Fluid Through a Row of Stationary Vanes.

The area of the control surface consists of the areas of the six sides of the prism ABCDEFGH and the surface area of the vanes profiles S_p . The region is the volume of the prism ABCDEFGH less the volume of the vanes. Inflow of the fluid at station 1 is through the surface S_1 , which is the

area enclosed by the rectangle ADHE. Outflow of fluid at station 2 is through the surface S_2 which is enclosed by the rectangle BCGF. The height of the prismatic control surface at station 1 is h_1 feet; at station 2 the height is h_2 feet. The unit vector normal to the surface at station 1 is \bar{n}_1 ; at station 2 it is \bar{n}_2 and on the profiles it is \bar{n}_p . Positive sense of these unit vectors is away from the control region. The unit vector parallel to the surface is \bar{t}_1 at station 1, \bar{t}_2 at station 2 and \bar{t}_p on the profiles. It is assumed that the control surface is completely filled with fluid and that there is a continuous velocity distribution within the region R.

Applying the momentum theorem between stations 1 and 2 gives

$$\frac{\partial}{\partial t} \left[\int_R d\bar{m} \bar{V} \right] + \int_{S_2} d\bar{m}_{S_2} \bar{V}_2 - \int_{S_1} d\bar{m}_{S_1} \bar{V}_1 = \int_S -\bar{n} p dS + \int_S -\bar{t} \tau dS + \bar{G} \quad (5)$$

For an assumed steady flow there is $\frac{\partial}{\partial t} \left[\int_R d\bar{m} \bar{V} \right] = 0$. For gases, such as air, the weight \bar{G} of the fluid within the control surface can be ignored with respect to the inertia forces. With $\bar{G} = 0$, Equation (5) becomes

$$\int_{S_2} d\bar{m}_{S_2} \bar{V}_2 - \int_{S_1} d\bar{m}_{S_1} \bar{V}_1 = \int_S -\bar{n} p dS + \int_S -\bar{t} \tau dS \quad (6)$$

The right-hand side of Equation (6) can be written

$$\begin{aligned} \int_S -\bar{n} p dS + \int_S -\bar{t} \tau dS = & \int_{S_1} -\bar{n}_1 p_1 dS_1 + \int_{S_2} -\bar{n}_2 p_2 dS_2 + \int_{S_p} -\bar{t}_1 \tau_1 dS_1 \\ & + \int_{S_2} -\bar{t}_2 \tau_2 dS_2 + \int_{S_p} -\bar{n}_p p_p dS_p + \int_{S_p} -\bar{t}_p \tau_p dS_p \end{aligned} \quad (7)$$

For regular velocity distributions the shear stress integrals at stations 1 and 2 can be ignored. The last two terms of Equation (7) represent the force exerted by the vane profiles on the fluid flow. The force \bar{F} exerted by the fluid flow on the vane profiles can be written

$$-\bar{F} = \int_{S_p} -\bar{\eta}_p \tau_p dS_p + \int_{S_p} -\bar{t}_p \tau_p dS_p \quad (8)$$

Using Equations (7) and (8) we can rewrite Equation (6)

$$\bar{F} = \int_{S_1} dm_{S_1} \bar{V}_1 - \int_{S_2} dm_{S_2} \bar{V}_2 + \int_{S_1} -\bar{\eta}_1 \tau_1 dS_1 + \int_{S_2} -\bar{\eta}_2 \tau_2 dS_2 \quad (9)$$

The force \bar{F} and the velocities \bar{V}_1 and \bar{V}_2 are vector quantities. In terms of their \bar{i} and \bar{j} components they are by definition

$$\bar{F} = \bar{i} F_a + \bar{j} F_u \quad (10)$$

$$\bar{V}_1 = \bar{i} V_{a1} + \bar{j} V_{u1} \quad (11)$$

$$\bar{V}_2 = \bar{i} V_{a2} + \bar{j} V_{u2} \quad (12)$$

The equations for an element of area at station 1 and at station 2 are

$$dS_1 = h_1 dx_1 \quad (13)$$

$$dS_2 = h_2 dx_2 \quad (14)$$

The mass flow rates through an element of area at stations 1 and 2 are obtained from

$$dm_{S_1} = h_1 \rho V_{a1} dx_1 \quad (15)$$

$$dm_{S_2} = h_2 \rho V_{a2} dx_2 \quad (16)$$

Utilizing the above relationships, Equation (9) becomes

$$\begin{aligned} \bar{i} F_a + \bar{j} F_u = & \int_0^{x_1} h_1 \rho V_{a_1} dx_1 (\bar{i} V_{a_1} + \bar{j} V_{u_1}) + \int_0^{x_1} \bar{i} h_1 p_1 dx_1 \\ & - \int_0^{x_2} \bar{i} h_2 p_2 dx_2 - \frac{\bar{i}(h_1 - h_2)}{2} \left[\int_0^{x_1} p_1 dx_1 + \int_0^{x_2} p_2 dx_2 \right] \\ & - \int_0^{x_2} h_2 \rho V_{a_2} dx_2 (\bar{i} V_{a_2} + \bar{j} V_{u_2}) \end{aligned} \quad (17)$$

Equating the \bar{i} components of Equation (17) we may write an expression for the axial component F_a of the force exerted by the fluid flow on the vanes. The \bar{j} components yield an expression for the tangential component F_u .

$$\begin{aligned} F_a = & \int_0^{x_1} h_1 \rho V_{a_1}^2 dx_1 + \int_0^{x_1} h_1 p_1 dx_1 - \int_0^{x_2} h_2 p_2 dx_2 \\ & - \frac{(h_1 - h_2)}{2} \left[\int_0^{x_1} p_1 dx_1 + \int_0^{x_2} p_2 dx_2 \right] \\ & - \int_0^{x_2} h_2 \rho V_{a_2}^2 dx_2 \end{aligned} \quad (18)$$

$$F_u = \int_0^{x_1} h_1 \rho V_{a_1} V_{u_1} dx_1 - \int_0^{x_2} h_2 \rho V_{a_2} V_{u_2} dx_2 \quad (19)$$

The magnitude of the force \bar{F} is obtained from the axial and tangential components by

$$F = \sqrt{(F_a)^2 + (F_u)^2} \quad (20)$$

Referring to Fig. 17, the angle between the force \bar{F} and the tangential direction is denoted by the symbol ϕ , and is found from

$$\phi = \tan^{-1} \frac{F_a}{F_u} \quad (21)$$

Equations (18) and (19), as written, determine the force exerted by the fluid flow on one test vane if the integration

is carried out over one vane spacing λ , or on λ test vanes if the integration is carried out over λ test vane spacings, λ not necessarily being an integer. Consequently, to determine the force exerted by the fluid flow on one test vane while carrying integration out over λ vane spacings, Equations (18) and (19) are modified as follows:

$$F_a = \frac{h_1 \rho}{\lambda_1} \int_0^{\lambda_1 \omega_1} V_{a_1}^2 dx_1 + \frac{h_1}{\lambda_1} \int_0^{\lambda_1 \omega_1} p_1 dx_1 - \frac{h_2}{\lambda_2} \int_0^{\lambda_2 \omega_2} p_2 dx_2 - \frac{(h_1 - h_2)}{2} \left[\frac{1}{\lambda_1} \int_0^{\lambda_1 \omega_1} p_1 dx_1 + \frac{1}{\lambda_2} \int_0^{\lambda_2 \omega_2} p_2 dx_2 \right] - \frac{h_2 \rho}{\lambda_2} \int_0^{\lambda_2 \omega_2} V_{a_2}^2 dx_2 \quad (22)$$

$$F_u = \frac{h_1 \rho}{\lambda_1} \int_0^{\lambda_1 \omega_1} V_{a_1} V_{u_1} dx_1 - \frac{h_2 \rho}{\lambda_2} \int_0^{\lambda_2 \omega_2} V_{a_2} V_{u_2} dx_2 \quad (23)$$

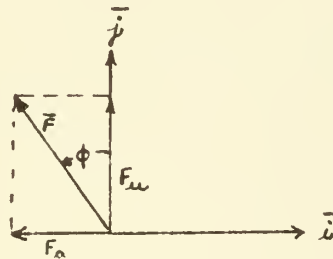


Figure 17. Illustration of the Angle ϕ .

5. Derivation of the Drag Coefficient of the Test Vanes.

Having established the force exerted by the fluid flow on one test vane and its relationship with respect to the vertical, the next step is to resolve this force into lift and drag components acting in perpendicular and parallel directions, respectively, to \bar{V}_{av} , the average of the velocities at stations 1 and 2, $\frac{\bar{V}_1 + \bar{V}_2}{2}$. Due to the fact that the velocities at stations 1 and 2 vary both in magnitude and direction along the test vane spacing at these stations, there is no suitable velocity upon which to base \bar{V}_{av} . A location in the fluid flow must be used where conditions of pressure, velocity and fluid flow angle do not vary in the direction of the test vane spacing. Such a reference location may be determined by the application of the momentum theorem between station 1 and a location upstream of station 1 where conditions of pressure, velocity and fluid flow angle are assumed to be uniform. This location is designated as station 0. With the continuity equation, the momentum equation may be solved for the pressure, velocity and fluid flow angle at station 0.

The same procedure can be employed to determine the conditions of pressure, velocity and fluid flow angle, also assumed to be constant in the direction of the test vane spacing, at a station far downstream of station 2 which is designated as station 3. The velocities \bar{V}_0 and \bar{V}_3 may then be added vectorially to obtain the average velocity \bar{V}_w to be used as the reference for the resolution of the force \bar{F} into lift and drag components.

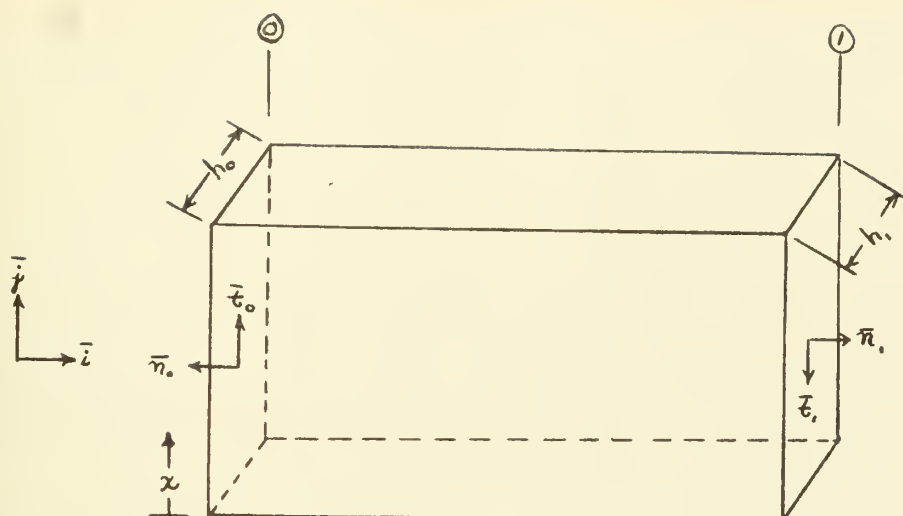


Figure 18. Control Surface for the Application of the Momentum Theorem Between Stations 0 and 1.

Figure 18 shows the control surface for the application of the momentum theorem between stations 0 and 1. With the same assumptions as used in the previous application of the momentum theorem, and noting that F_a and F_u are zero between stations 0 and 1, and that $h_0 = h_1$, we can rewrite Equations (22) and (23)

$$\frac{h_0}{\lambda_0} \int_0^{\lambda_0} \rho_0 dx_0 - \frac{h_1}{\lambda_1} \int_0^{\lambda_1} \rho_1 dx_1 + \frac{h_0 \rho}{\lambda_0} \int_0^{\lambda_0} V_{a_0}^2 dx_0 - \frac{h_1 \rho}{\lambda_1} \int_0^{\lambda_1} V_{a_1}^2 dx_1 = 0 \quad (24)$$

$$\frac{h_0 \rho}{\lambda_0} \int_0^{\lambda_0} V_{a_0} V_{w_0} dx_0 - \frac{h_1 \rho}{\lambda_1} \int_0^{\lambda_1} V_{a_1} V_{w_1} dx_1 = 0 \quad (25)$$

By assumption V_{a_0} , V_{w_0} and ρ_0 do not vary; therefore we may simplify Equations (24) and (25)

$$h_0 \rho_0 x_0 - \frac{h_1}{\lambda_1} \int_0^{\lambda_1} \rho_1 dx_1 + h_0 \rho V_{a_0}^2 x_0 - \frac{h_1 \rho}{\lambda_1} \int_0^{\lambda_1} V_{a_1}^2 dx_1 = 0 \quad (26)$$

$$h_0 \rho V_{a_0} V_{w_0} x_0 - \frac{h_1 \rho}{\lambda_1} \int_0^{\lambda_1} V_{a_1} V_{w_1} dx_1 = 0 \quad (27)$$

The velocity V_{a_0} may be determined by the application of the continuity equation between station 0 and 1.

$$\begin{aligned}
 m_{s_0} &= m_{s_1} \\
 \rho h_0 V_{a_0} x_0 &= \frac{h_1 \rho}{\lambda_1} \int_0^{\lambda_1 x_1} V_{a_1} dx_1 \\
 V_{a_0} &= \frac{\frac{h_1 \rho}{\lambda_1} \int_0^{\lambda_1 x_1} V_{a_1} dx_1}{\rho h_0 x_0}
 \end{aligned} \tag{28}$$

Equation (26) can now be solved for

$$\tau_0 = \frac{\frac{h_1 \rho}{\lambda_1} \int_0^{\lambda_1 x_1} p_1 dx_1 - h_0 \rho V_{a_0}^2 x_0 + \frac{h_1 \rho}{\lambda_1} \int_0^{\lambda_1 x_1} V_{a_1}^2 dx_1}{h_0 x_0} \tag{29}$$

From Equation (27)

$$V_{u_0} = \frac{\frac{h_1 \rho}{\lambda_1} \int_0^{\lambda_1 x_1} V_{a_1} V_{u_1} dx_1}{h_0 \rho V_{a_0} x_0} \tag{30}$$

Referring to Fig. 19, the angle between \bar{V}_0 and the horizontal, β_0 , is by definition

$$\beta_0 = \tan^{-1} \frac{V_{u_0}}{V_{a_0}} \tag{31}$$

The magnitude of the velocity \bar{V}_0 is found from the axial and tangential components by

$$V_0 = \sqrt{(V_{a_0})^2 + (V_{u_0})^2} \tag{32}$$

The momentum theorem is applied between stations 2 and 3 in the same manner as between stations 0 and 1. The results are

$$V_{a_3} = \frac{\frac{h_2 \rho}{\lambda_2} \int_0^{\lambda_2 x_2} V_{a_2} dx_2}{\rho h_3 x_3} \tag{33}$$

$$p_3 = \frac{\frac{h_2}{\lambda_2} \int_0^{\lambda_2 \mu_2} \tau_2^2 dx_2 - h_3 \rho V_{a_3}^2 x_3 + \frac{h_2 \rho}{\lambda_2} \int_0^{\lambda_2 \mu_2} V_{a_2}^2 dx_2}{h_3 x_3} \quad (34)$$

$$V_{u_3} = \frac{\frac{h_2 \rho}{\lambda_2} \int_0^{\lambda_2 \mu_2} V_{a_2} V_{u_2} dx_2}{h_3 \rho V_{a_3} x_3} \quad (35)$$

$$\beta_3 = \tan^{-1} \frac{V_{u_3}}{V_{a_3}} \quad (36)$$

$$V_3 = \sqrt{(V_{a_3})^2 + (V_{u_3})^2} \quad (37)$$

Figure 19 illustrates the relationship of the velocities \bar{V}_0 , \bar{V}_3 and \bar{V}_∞ , and the resolution of the force \bar{F} into lift and drag components.

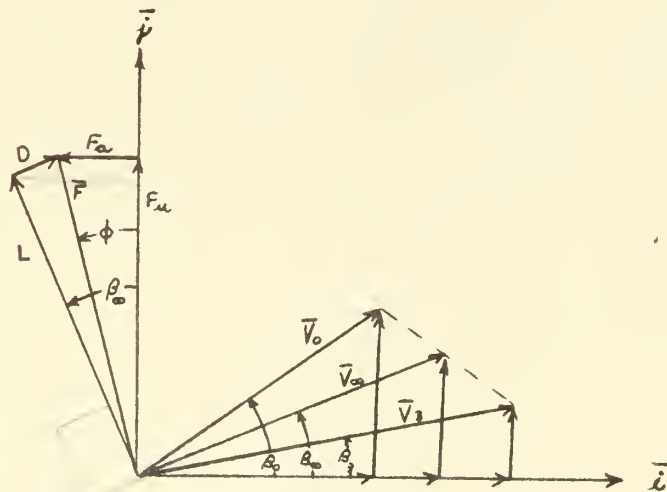


Figure 19. Illustration of the Velocities \bar{V}_0 , \bar{V}_3 and \bar{V}_∞ , and the Resolution of the Force \bar{F} into Lift and Drag Components.

The velocity \bar{V}_∞ is

$$\begin{aligned}\bar{V}_\infty &= \frac{\bar{V}_0 + \bar{V}_3}{2} \\ \bar{V}_\infty &= \bar{i} V_{u_\infty} + \bar{j} V_{w_\infty} \\ \bar{V}_\infty &= \frac{\bar{i} (V_{u_0} + V_{u_3}) + \bar{j} (V_{w_0} + V_{w_3})}{2}\end{aligned}\quad (38)$$

The angle between \bar{V}_∞ and the horizontal, shown in Fig. 19, is

$$\beta_\infty = \tan^{-1} \frac{V_{w_\infty}}{V_{u_\infty}} \quad (39)$$

The following expressions for the lift and drag force acting on a test vane can be determined from Fig. 19.

$$L = F \cos (\beta_\infty - \phi) \quad (40)$$

$$D = F \sin (\beta_\infty - \phi) \quad (41)$$

The equations for the coefficients of lift and drag are

$$C_L = \frac{L}{\frac{1}{2} \rho h_{av} \infty V_\infty^2} \quad (42)$$

$$C_D = \frac{D}{\frac{1}{2} \rho h_{av} \infty V_\infty^2} \quad (43)$$

where

$$h_{av} = \frac{h_0 + h_3}{2} \quad (44)$$

6. Derivation of the Drag Coefficient from Thermodynamic Relationships.

In this section a relationship for the drag coefficient will be derived with thermodynamic relations which will then be modified for applications to incompressible flows. With these derivations it shall be shown that the data obtained for incompressible flows in cascade test rigs can be used for compressible flows also, as long as the Mach numbers are small.

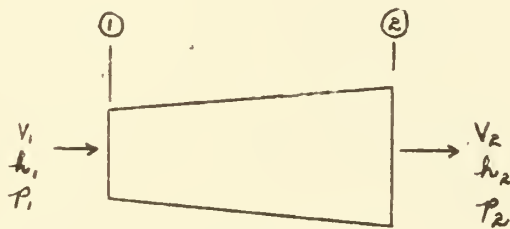


Figure 20. System for Calculating Energy Relations in Flow.

For the system shown in Fig. 20, it can be shown that the general energy equation for steady flows can be written as

$$q = h_2 - h_1 + \frac{1}{2} V_1^2 - \frac{1}{2} V_2^2 \quad (45)$$

Where q is the heat exchanged between the system and its surroundings, h_1 is the enthalpy of the fluid at station 1, h_2 is the enthalpy of the fluid at station 2, V_1 is the velocity of the fluid at station 1, and V_2 is the velocity of the fluid at station 2. For adiabatic flow where $q = 0$, there is from Equation (45)

$$h_2 + \frac{1}{2} V_2^2 = h_1 + \frac{1}{2} V_1^2 \quad (46)$$

For steady, adiabatic flows, and ignoring gravity effects, there is

$$h + \frac{1}{2} V^2 = \text{constant} \quad (47)$$

For perfect gases

$$C_p T + \frac{1}{2} V^2 = \text{constant} = C_p T_s \quad (48)$$

where C_p is the specific heat at constant pressure of the fluid and T_s is the reservoir, or stagnation, temperature.

Additionally, for isentropic flow

$$\frac{p}{p_s} = \left(\frac{\rho}{\rho_s} \right)^\gamma = \left(\frac{T}{T_s} \right)^{\frac{\gamma}{\gamma-1}} \quad (49)$$

where the unsubscripted values of pressure, density and temperature refer to local values at some point in the fluid flow, and the subscript s refers to the stagnation, or reservoir, values. γ is the ratio of specific heats c_p/c_v .

To express the ratio p/ρ_s for non-isentropic flows, the relationship $a^2 = \gamma R_g T$ for the speed of sound is substituted in Equation (48)

$$\frac{V^2}{2} + \frac{a^2}{\gamma-1} = \frac{a_s^2}{\gamma-1} \quad (50)$$

where R_g is the gas constant of the fluid.

Multiplying Equation (50) by $\frac{\gamma-1}{a^2}$

$$\frac{a_s^2}{a^2} = \frac{T_s}{T} = 1 + \frac{\gamma-1}{2} M^2 \quad (51)$$

With Equation (51), the expressions for isentropic processes of Equation (49) are

$$\frac{p_s}{p} = \left(1 + \frac{\gamma-1}{2} M^2 \right)^{\frac{\gamma}{\gamma-1}} \quad (52)$$

$$\frac{p_s}{p} = \left(1 + \frac{\gamma-1}{2} M^2\right)^{\frac{\gamma}{\gamma-1}} \quad (53)$$

where M is the Mach number V/a .

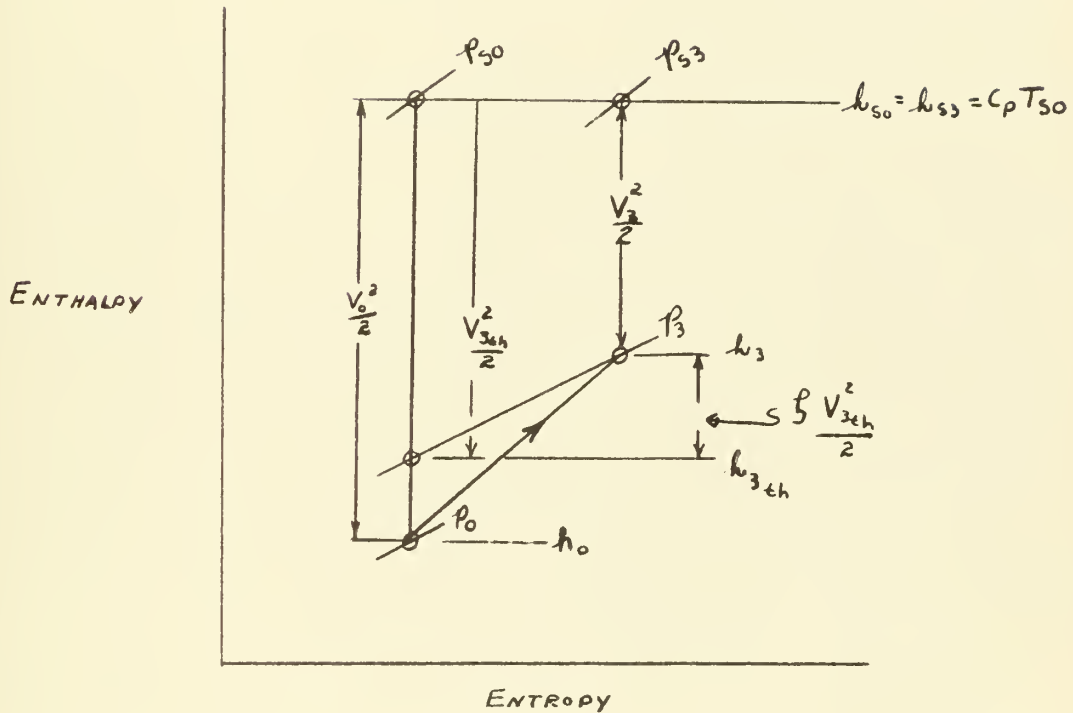


Figure 21. An Enthalpy-Entropy Diagram of the Fluid Through Cascade for Decelerated Flow.

An enthalpy-entropy diagram representing the conditions of state of the fluid through the cascade is shown in Fig. 21. The static pressure at station 0 is p_0 , at station 3 it is p_3 . The stagnation, or reservoir, pressure is p_{s0} at station 0 and p_{s3} at station 3. For adiabatic conditions, the total enthalpy h_s remains constant between stations 0 and 3 as no energy is added to or dissipated

$$P_{s3} = P_3 \left(1 + \frac{\gamma}{2} \frac{V_3^2}{a_{s0}^2} \right) \quad (60)$$

$$P_{s0} = P_3 \left(1 + \frac{\gamma}{2\eta} \frac{V_3^2}{a_{s0}^2} \right) \quad (61)$$

Subtracting Equation (60) from Equation (61)

$$P_{s0} - P_{s3} = \frac{P_3 \gamma}{2 a_{s0}^2} \left(\frac{V_3^2}{\eta} - V_3^2 \right) \quad (62)$$

Using $a_{s0}^2 = \gamma R_g T_{s0}$, Equation (62) is

$$P_{s0} - P_{s3} = \frac{P_3 V_3^2}{R_g T_{s0}} \left(\frac{1}{\eta} - 1 \right) \quad (63)$$

With $P = \rho R_g T$, Equation (63) is

$$P_{s0} - P_{s3} = \frac{\rho V_3^2}{2} \left(\frac{1}{\eta} - 1 \right) \quad (64)$$

Solving Equation (64) for $\left(\frac{1}{\eta} - 1 \right)$

$$\left(\frac{1}{\eta} - 1 \right) = \frac{(P_{s0} - P_{s3})}{\frac{\rho}{2} V_3^2} = \xi \quad (65)$$

Multiplying Equation (65) by η

$$(1 - \eta) = \frac{\eta(P_{s0} - P_{s3})}{\frac{\rho}{2} V_3^2} = \eta \xi \quad (66)$$

Using Equation (55), Equation (66) is

$$(1 - \eta) = \frac{(P_{s0} - P_{s3})}{\frac{\rho}{2} V_{3ch}^2} \quad (67)$$

With Equation (67), Equation (56) is

$$\xi = \frac{(P_{s0} - P_{s3})}{\frac{\rho}{2} V_{3ch}^2} = \eta \xi \quad (68)$$

from the flow. If the fluid flow were frictionless between station 0 and 3, the exit kinetic energy of the fluid would be $\frac{V_{3\epsilon h}^2}{2}$. However, with friction, the exit kinetic energy of the fluid flow will be smaller, say, equal to $\frac{V_3^2}{2}$. The loss of kinetic energy due to friction can be represented by the loss coefficient

$$\zeta = \frac{V_{3\epsilon h}^2 - V_3^2}{V_{3\epsilon h}^2} \quad (54)$$

Further, introducing the blading efficiency η , where

$$\eta = \frac{V_3^2}{V_{3\epsilon h}^2} \quad (55)$$

there is
$$\zeta = 1 - \eta \quad (56)$$

The static pressure and the velocities may be related by using Equation (52) along the respective lines of constant entropy.

$$\frac{p_{s3}}{p_3} = \left(1 + \frac{\gamma-1}{2} M_3^2\right)^{\frac{\gamma}{\gamma-1}} = \left(1 + \frac{\gamma-1}{2} \frac{V_3^2}{a_3^2}\right)^{\frac{\gamma}{\gamma-1}} \quad (57)$$

$$\frac{p_{s0}}{p_3} = \left(1 + \frac{\gamma-1}{2} M_{3\epsilon h}^2\right)^{\frac{\gamma}{\gamma-1}} = \left(1 + \frac{\gamma-1}{2} \frac{V_{3\epsilon h}^2}{a_{3\epsilon h}^2}\right)^{\frac{\gamma}{\gamma-1}} \quad (58)$$

Using Equation (55), Equation (58) is

$$\frac{p_{s0}}{p_3} = \left(1 + \frac{\gamma-1}{2} \frac{V_3^2}{\eta a_3^2}\right)^{\frac{\gamma}{\gamma-1}} \quad (59)$$

For incompressible flow $\rho = \rho_0 = \rho_3$, and $a_3 \cong a_{3\epsilon h} \cong a_{s0}$. Equations (57) and (59), of the form $(1+x)^n$, can be expanded by a binomial series. Neglecting terms of x^2 and higher powers of x ,

From Fig. 19 and the application of the momentum theorem between stations 0 and 3, for $\alpha_0 = \alpha_3 = \alpha$ and $h_{av} = \frac{h_0 + h_3}{2}$

$$F_x = L \sin \beta_\infty - D \cos \beta_\infty = \alpha h_{av} (P_3 - P_0) + \int \alpha (h_3 V_{a_3}^2 - h_0 V_{a_0}^2) \quad (69)$$

$$F_y = L \cos \beta_\infty + D \sin \beta_\infty = \alpha \int (h_0 V_{a_0} V_{w_0} - h_3 V_{a_3} V_{w_3}) \quad (70)$$

Multiplying Equation (69) by $-\cos \beta_\infty$ and Equation (70) by $\sin \beta_\infty$ and adding

$$\begin{aligned} D = & \alpha h_{av} (P_0 - P_3) \cos \beta_\infty - \int \alpha (h_3 V_{a_3}^2 - h_0 V_{a_0}^2) \cos \beta_\infty \\ & + \alpha \int (h_0 V_{a_0} V_{w_0} - h_3 V_{a_3} V_{w_3}) \sin \beta_\infty \end{aligned} \quad (71)$$

With $D = C_D \rho_{\frac{1}{2}} V_\infty^2 \frac{c}{\alpha}$ Equation (71), after dividing by $h_{av} \alpha$, is

$$\begin{aligned} C_D \rho_{\frac{1}{2}} V_\infty^2 \frac{c}{\alpha} = & (P_0 - P_3) \cos \beta_\infty - \int \left(\frac{h_3}{h_{av}} V_{a_3}^2 - \frac{h_0}{h_{av}} V_{a_0}^2 \right) \cos \beta_\infty \\ & + \int \left(\frac{h_0}{h_{av}} V_{a_0} V_{w_0} - \frac{h_3}{h_{av}} V_{a_3} V_{w_3} \right) \sin \beta_\infty \end{aligned} \quad (72)$$

Solving for $(P_0 - P_3)$ from Equation (65)

$$\xi = \frac{(P_{s0} - P_{s3})}{\rho_{\frac{1}{2}} V_3^2} = \frac{(P_0 - P_3) + \rho_{\frac{1}{2}} (V_0^2 - V_3^2)}{\rho_{\frac{1}{2}} V_3^2}$$

or

$$(P_0 - P_3) = \xi \rho_{\frac{1}{2}} V_3^2 - \rho_{\frac{1}{2}} (V_0^2 - V_3^2) \quad (73)$$

Substituting Equation (73) in Equation (72) and dividing by $\rho_{\frac{1}{2}}$

$$\begin{aligned} C_D V_\infty^2 \frac{c}{\alpha} = & \xi V_3^2 \cos \beta_\infty - (V_0^2 - V_3^2) \cos \beta_\infty \\ & - 2 \left(\frac{h_3}{h_{av}} V_{a_3}^2 - \frac{h_0}{h_{av}} V_{a_0}^2 \right) \cos \beta_\infty \\ & + 2 \left(\frac{h_0}{h_{av}} V_{a_0} V_{w_0} - \frac{h_3}{h_{av}} V_{a_3} V_{w_3} \right) \sin \beta_\infty \end{aligned} \quad (74)$$

From the continuity equation, the mass flow rate must be the same at all stations.

$$m_{s0} = m_{s1} = m_{s\infty}$$

$$h_0 V_{a0} = h_1 V_{a1} = h_{av} V_{av}$$

$$V_{av} = \frac{h_0}{h_{av}} V_{a0} = \frac{h_1}{h_{av}} V_{a1} \quad (75)$$

With Equation (75) and dividing by V_∞^2 , Equation (74) is

$$C_D \frac{C}{A} = \left\{ \frac{V_3^2}{V_\infty^2} \cos \beta_\infty - \frac{(V_0^2 - V_3^2)}{V_\infty^2} \cos \beta_\infty \right. \\ \left. - 2 \frac{V_{a0}}{V_\infty^2} (V_{a3} - V_{a0}) \cos \beta_\infty + 2 \frac{V_{a0}}{V_\infty^2} (V_{w0} - V_{w3}) \sin \beta_\infty \right\} \quad (76)$$

Substituting $V_0^2 = V_{a0}^2 + V_{w0}^2$

$$V_3^2 = V_{a3}^2 + V_{w3}^2$$

and $V_{a0} = V_\infty \cos \beta_\infty$, Equation (76) is

$$C_D \frac{C}{A} = \left\{ \frac{V_3^2}{V_\infty^2} \cos \beta_\infty - \frac{(V_{a0}^2 + V_{w0}^2 - V_{a3}^2 - V_{w3}^2)}{V_\infty^2} \cos \beta_\infty \right. \\ \left. - 2 \frac{V_{a0}}{V_\infty^2} (V_{a3} - V_{a0}) \cos \beta_\infty + \frac{2}{V_\infty^2} (V_{w0} - V_{w3}) V_\infty \cos \beta_\infty \sin \beta_\infty \right\} \quad (77)$$

Substituting $V_\infty^2 = \frac{V_{a0}^2}{\cos^2 \beta_\infty}$ in all terms and $V_{w0} = V_\infty \sin \beta_\infty$

in the last term, Equation (77) is

$$C_D \frac{C}{A} = \left\{ \frac{\cos^3 \beta_\infty}{V_{a0}^2} \left[V_3^2 - (V_{a0}^2 + V_{w0}^2 - V_{a3}^2 - V_{w3}^2) \right. \right. \\ \left. \left. - 2 V_{a0} (V_{a3} - V_{a0}) + 2 V_{w0} (V_{w0} - V_{w3}) \right] \right\} \quad (78)$$

?
 $\frac{C}{A}$ is just for first term

With $V_{a0} = \frac{V_{a0} + V_{a3}}{2}$, $V_{w0} = \frac{V_{w0} + V_{w3}}{2}$, Equation (78) can be expanded to give the result

$$C_D = \left\{ \frac{V_3^2 \cos^3 \beta_\infty}{\frac{C}{A} V_{a0}^2} \right\} \quad (79)$$

Substituting the solidity of the cascade $\sigma = \frac{c}{d}$ and

$$V_{\alpha\infty}^2 = V_\infty^2 \cos^2 \beta_\infty, \quad \text{Equation (79) is}$$

$$C_D = \frac{c}{\sigma} \left(\frac{V_3}{V_\infty} \right)^2 \cos \beta_\infty \quad (80)$$

The drag coefficients obtained from Equation (80) for incompressible flows can be used for compressible flows if Mach numbers are small. Table I shows the exact value of P_{s3}/P_3 calculated from Equation (57) and the approximate value of P_{s3}/P_3 calculated from Equation (60). Also shown is the approximate value of P_{s3}/P_3 minus the exact value of P_{s3}/P_3 .

TABLE I
COMPARISON OF APPROXIMATE AND EXACT VALUES OF P_{53}/P_3

M	M ²	P_{53}/P_3		APPROX. MINUS EXACT
		EXACT	APPROX.	
0.05	0.0025	1.0001	1.0018	0.0017
0.10	0.0100	1.0006	1.0070	0.0064
0.15	0.0225	1.0011	1.0158	0.0147
0.20	0.0400	1.0023	1.0280	0.0257
0.25	0.0625	1.0036	1.0438	0.0402
0.30	0.0900	1.0051	1.0630	0.0582
0.35	0.1225	1.0069	1.0858	0.0789
0.40	0.1600	1.0091	1.1120	0.1129
0.45	0.2025	1.0104	1.1418	0.1314

7. Data Required for Determination of Cascade Performance.

The equations derived in the preceding sections may be solved knowing the values of static pressure P and the quantities V , V_a , V_w and V_a^2 . Introducing the total pressure

$$P_s = P + \frac{\rho}{2} V^2 \quad (81)$$

there is

$$V^2 = \frac{2}{\rho} (P_s - P) \quad (82)$$

From Fig. 22,

$$V_a = V \cos \alpha \quad (83)$$

$$V_w = V \sin \alpha \quad (84)$$

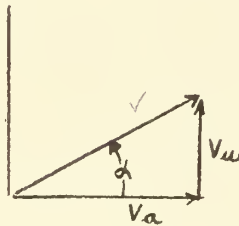


Figure 22. Relationship of Velocity V and Angle of Fluid Flow α .

From Equations (82), (83), and (84),

$$V_a^2 = V^2 \cos^2 \alpha = \frac{2}{\rho} (P_s - P) \cos^2 \alpha \quad (85)$$

$$V_a V_w = V^2 \cos \alpha \sin \alpha = \frac{2}{\rho} (P_s - P) \cos \alpha \sin \alpha \quad (86)$$

Values of static pressure P , total pressure P_s and the angle of fluid flow α were measured at station 1 which is located between the inlet guide vanes and the test vanes, and at station 2 downstream of the test vanes. Measurements were taken at blade heights of one-quarter, one-half and three-quarters.

8. Static Pressure Distribution in the Cascade.

It is essential that the static pressure distribution ahead of the test vanes is constant from upper wall to lower wall. Therefore, prior to mounting the cascade on the nozzle block, surveys of total pressure P_0 and dynamic pressure P_D were taken in a vertical plane at the discharge of the rectangular nozzle, that is, without guide and test vanes. The initial survey, shown in Fig. 23, indicated several regions of irregularity in the profiles. These irregularities were removed by increasing the resistance encountered by the fluid flow at the diffuser discharge. This was accomplished by placing additional screens of finer mesh between the diffuser discharge and the inlet to the settling chamber. Details of the screens are shown in Fig. 24. Initially, two 40 mesh per inch screens were placed between the diffuser discharge and the settling chamber inlet. The final pressure profile, shown in Fig. 25, was determined with the following screen arrangements: one 100 mesh per inch screen, two 80 mesh per inch screens and two 40 mesh per inch screens.

The cascade was mounted on the discharge face of the nozzle block. Surveys of total and static pressure were taken between the inlet guide vanes and the test vanes. Plots of the total and static pressures from the first sets of data revealed that the static pressure distribution ahead of the test vanes was not uniform. As shown in Fig. 26, the static pressure varied from a value of a minus one inch of water to above zero inches of water. At this point the test

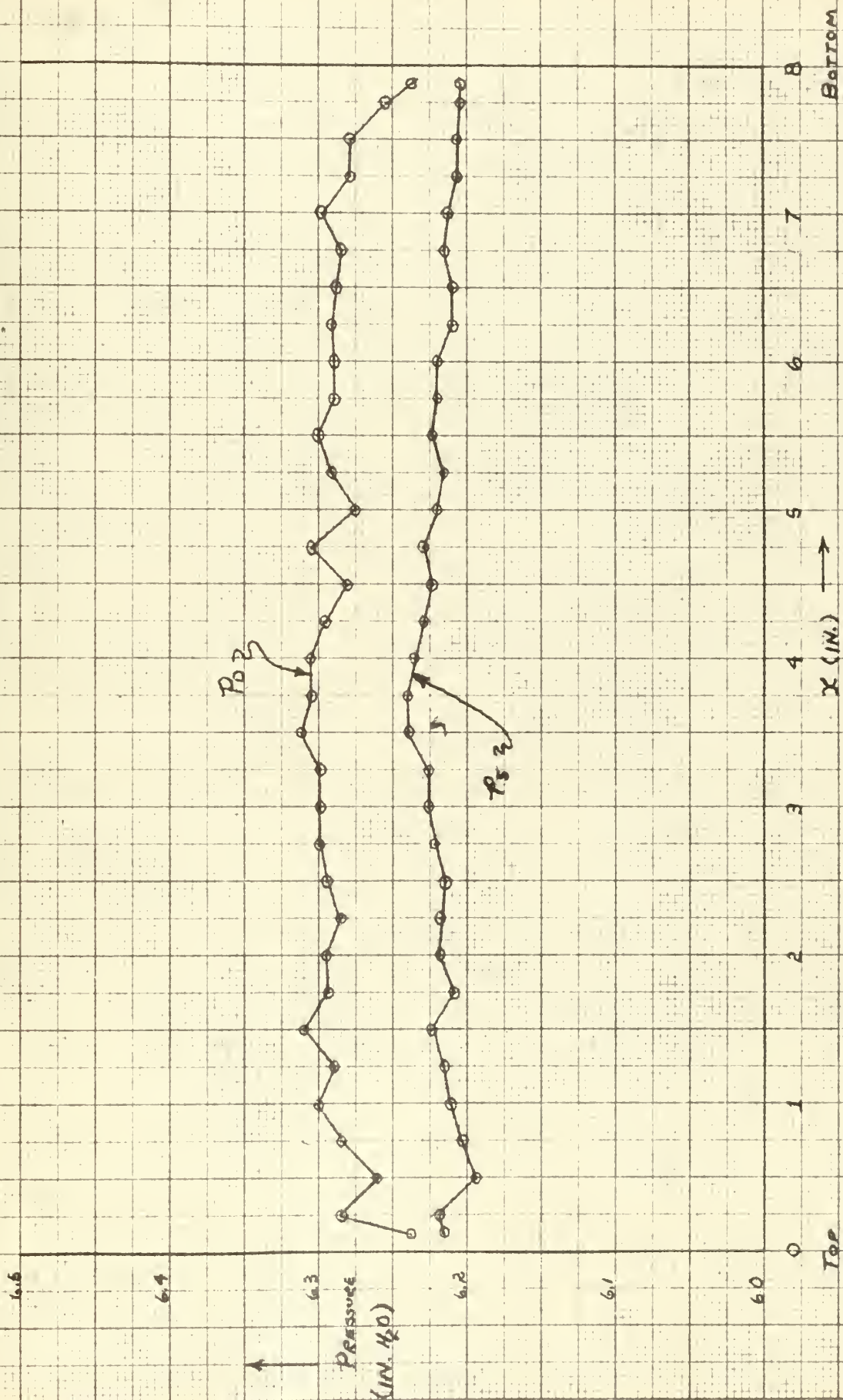
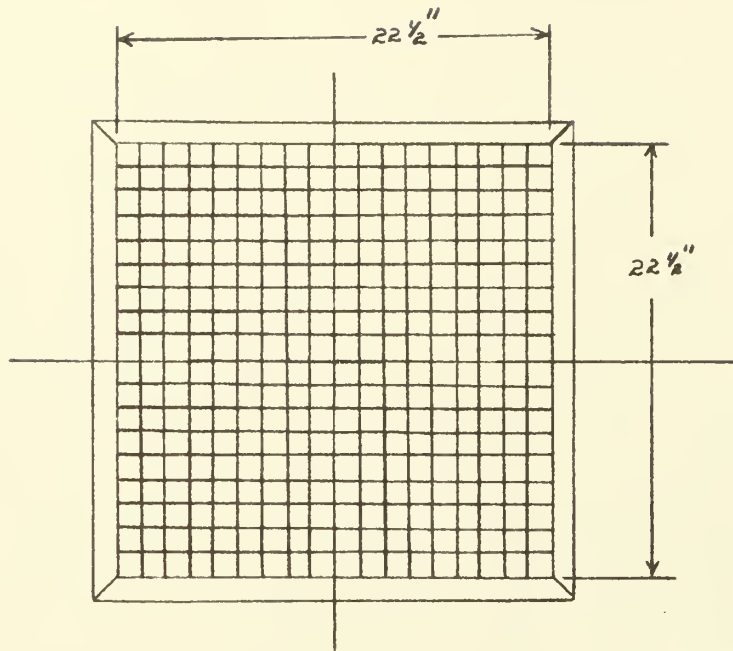


FIGURE 23. INITIAL PRESSURE SURVEY. PROBE 4" FROM NOZZLE.



MESH DETAIL

No.	MESH PER INCH	WIRE DIAMETER
1	40	.0091 IN.
2	80	.0058 IN.
3	100	.0035 IN.

FIGURE 24. SCREEN DETAILS.

6.5

6.4

6.3

6.2

6.1

6.0

0

Top

PRESSURE
(IN. H₂O)

P03

P22

2

3

4

5

6

7

8

Bottom

X (IN.)

FIGURE 25. FINAL PRESSURE SURVEY. PROBE 1/2" FROM NOZZLES

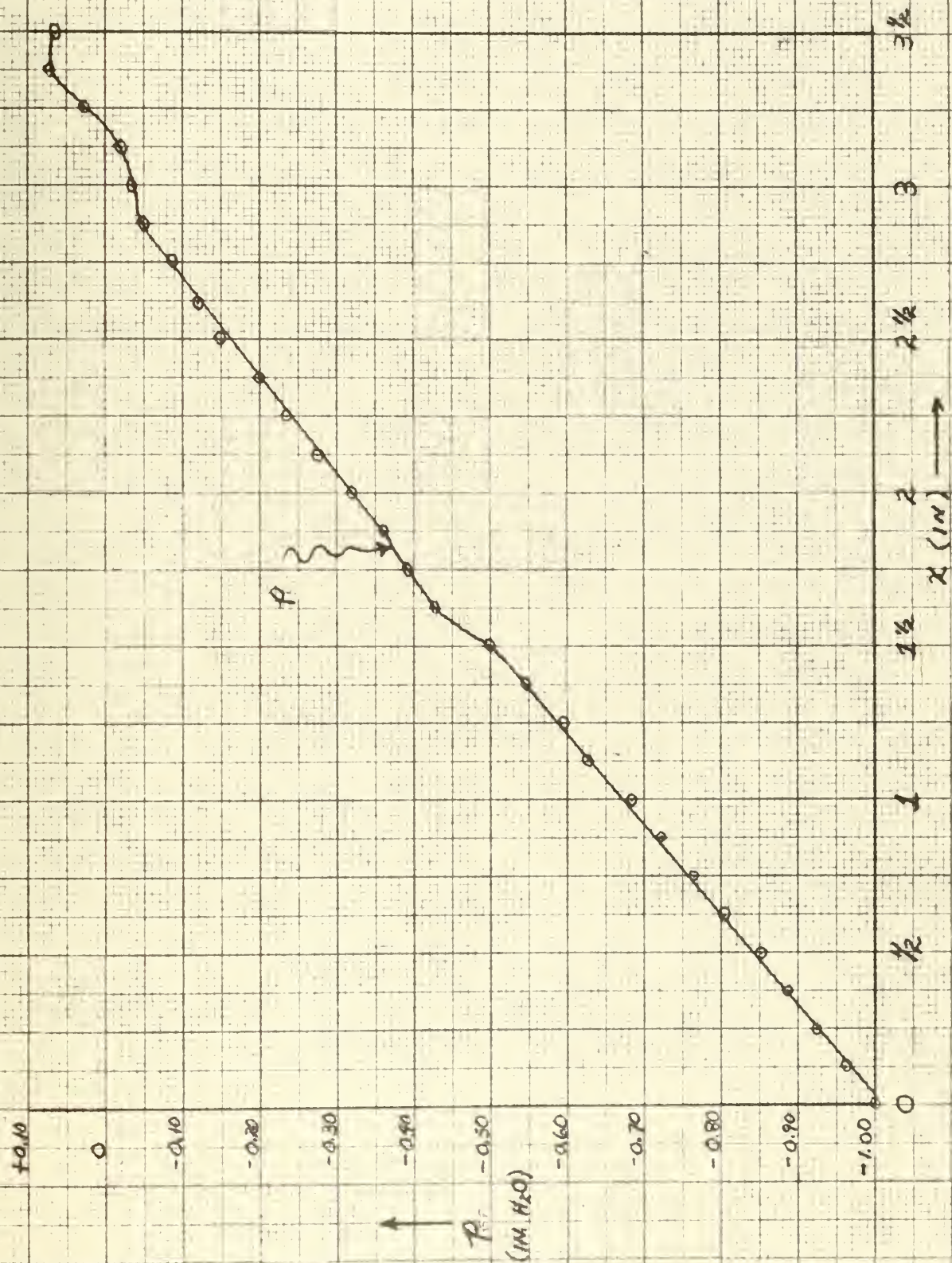


FIGURE 26. STATIC PRESSURE PROFILE @ $h = \frac{1}{2}$ BLADE HEIGHT.

vanes were removed from the cascade and data were taken to determine the static pressure after the inlet guide vanes. These data, shown in Fig. 27, again revealed an unsatisfactory static pressure profile. Assuming the difficulty in obtaining the proper static pressure profile to be associated with the contour of the upper and lower walls, these walls were removed and the static pressure profile after the inlet guide vanes was measured to find out how it differed from that originally measured with the entire cascade removed. Plots of these data were favorable, indicating a region of constant static pressure extending about two inches on either side of the center of the cascade.

Having thus determined that the contour of the upper and lower walls largely determined the profile of the static pressure, it was set about to find the influence of various wall contours on the static pressure profiles. This was accomplished by holding the contour of the upper wall fixed while varying the contour of the lower wall. When a satisfactory static pressure profile was obtained over the lower portion of the channel, the contour of the lower wall was held fixed and the contour of the upper wall was varied. Using this procedure it was possible to obtain a satisfactory static pressure profile over the majority of the test area with the test vanes removed. Figure 28 shows the effect of varying the contour of the lower wall while holding the contour of the upper wall fixed. The notation 11 and 5 used in these figures refers to upper wall contour 11 and lower wall

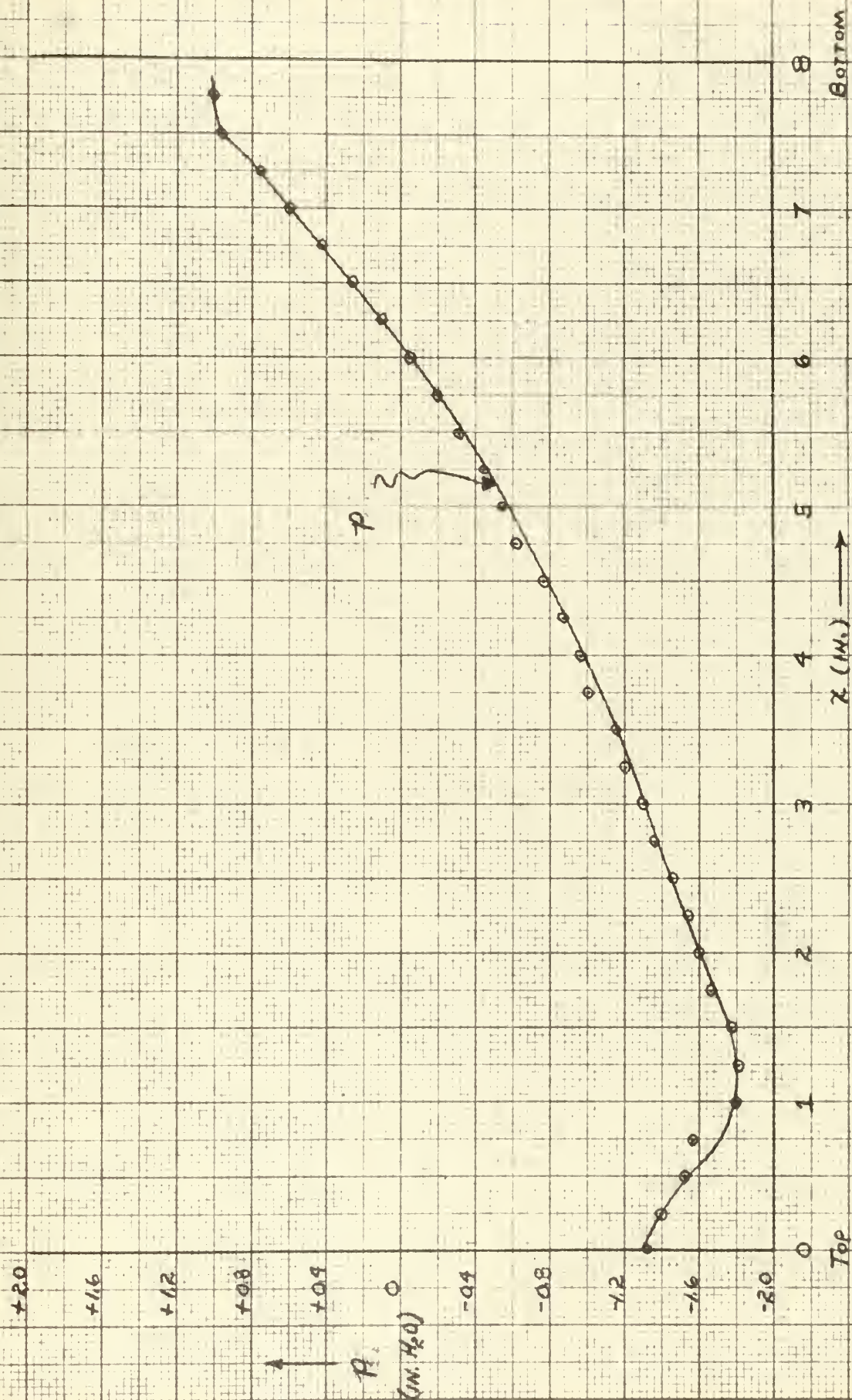


FIGURE 27. STATIC PRESSURE PROFILE @ $A_1 = \frac{1}{2}$ BLADE HEIGHT.
TEST VANES REMOVED.

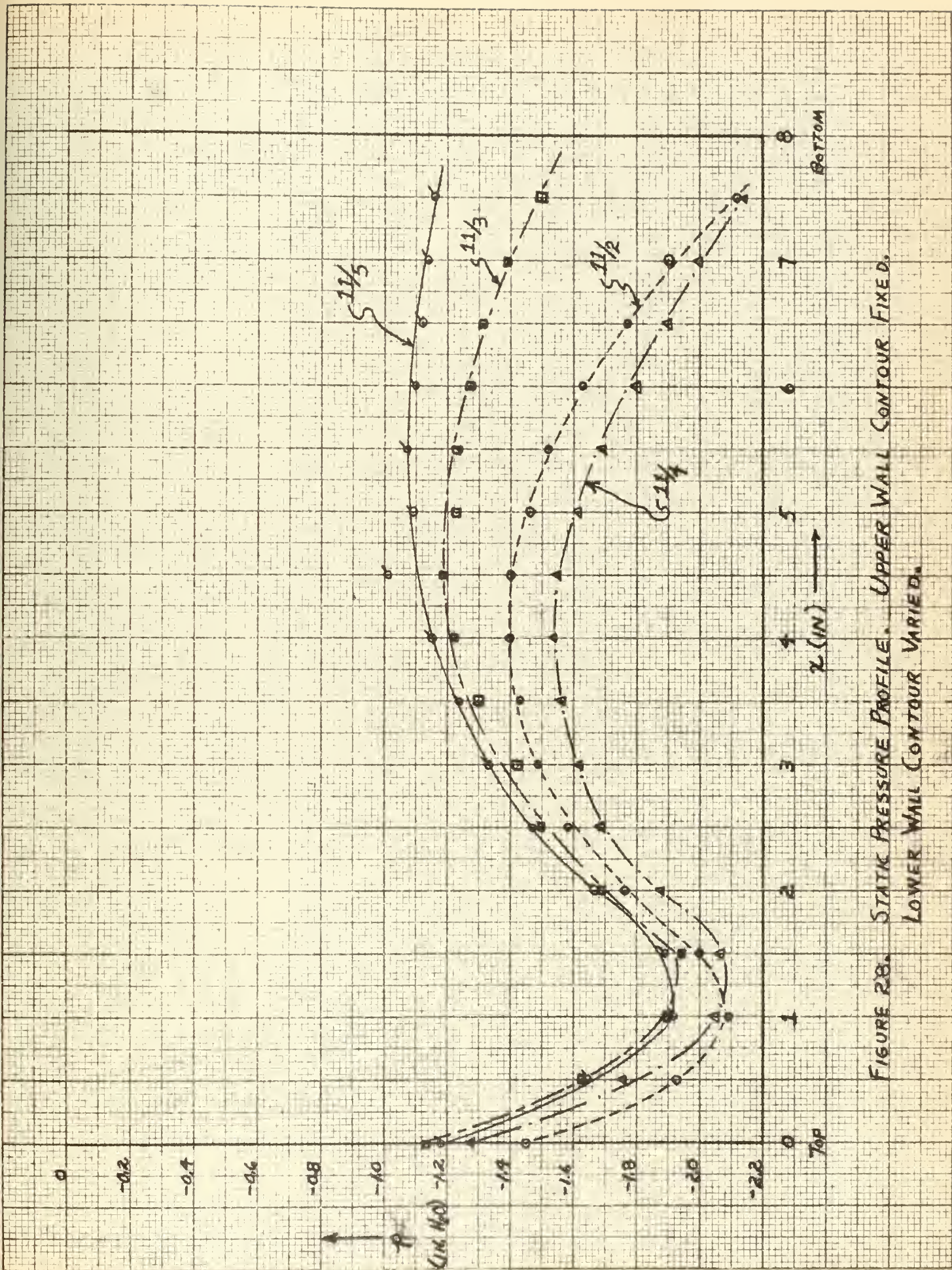


FIGURE 28. STATIC PRESSURE PROFILE. UPPER WALL CONTOUR FIXED, LOWER WALL CONTOUR VARIED.

contour 5, respectively. Figure 29 shows the various lower wall contours used. From Fig. 28 and Fig. 29 it is seen that decreasing the distance between the upper and lower walls increases the static pressure over the bottom four inches of the channel, but has little effect on the static pressure over the upper four inches of the cascade. Increasing the slope of the lower wall has the effect of bringing the contour of the lower wall closer to the streamlines of the fluid flow at the bottom of the channel. The expansion of the fluid is thus reduced, resulting in a static pressure increase.

Figure 30 shows the effect of varying the contour of the upper wall while holding the contour of the lower wall fixed. Figure 31 shows the contours of the various upper wall contours used. From Fig. 30 and Fig. 31 it is seen that decreasing the slope of the upper wall, thus bringing the contour of the upper wall closer to the streamlines of the fluid flow at the top of the cascade, had its major effect on the upper four inches of the channel. It also decreased slightly the static pressure at the bottom of the cascade. Additional adjustment of the contour of the upper and lower wall resulted in a satisfactory static pressure profile. For the cascade investigations the contours 14 and 6 were used for upper and lower walls, respectively.

At this juncture the test vanes were reinstalled in the cascade and a profile of static pressure was obtained after the inlet guide vanes. This profile, shown in Fig. 32, again was unsatisfactory. It can be seen from this figure

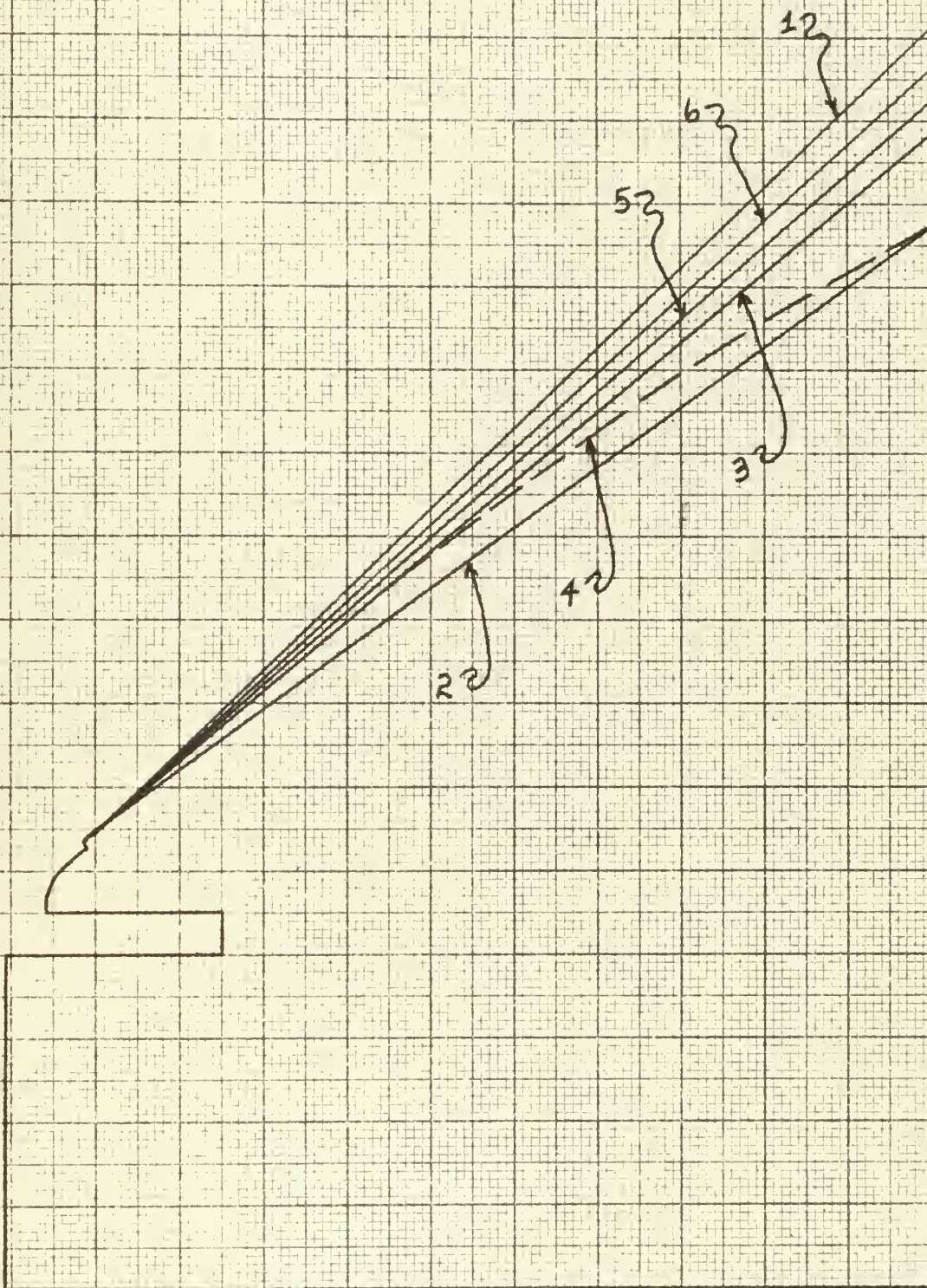


FIGURE 29. LOWER WALL CONTOURS. SCALE: FULL SIZE.

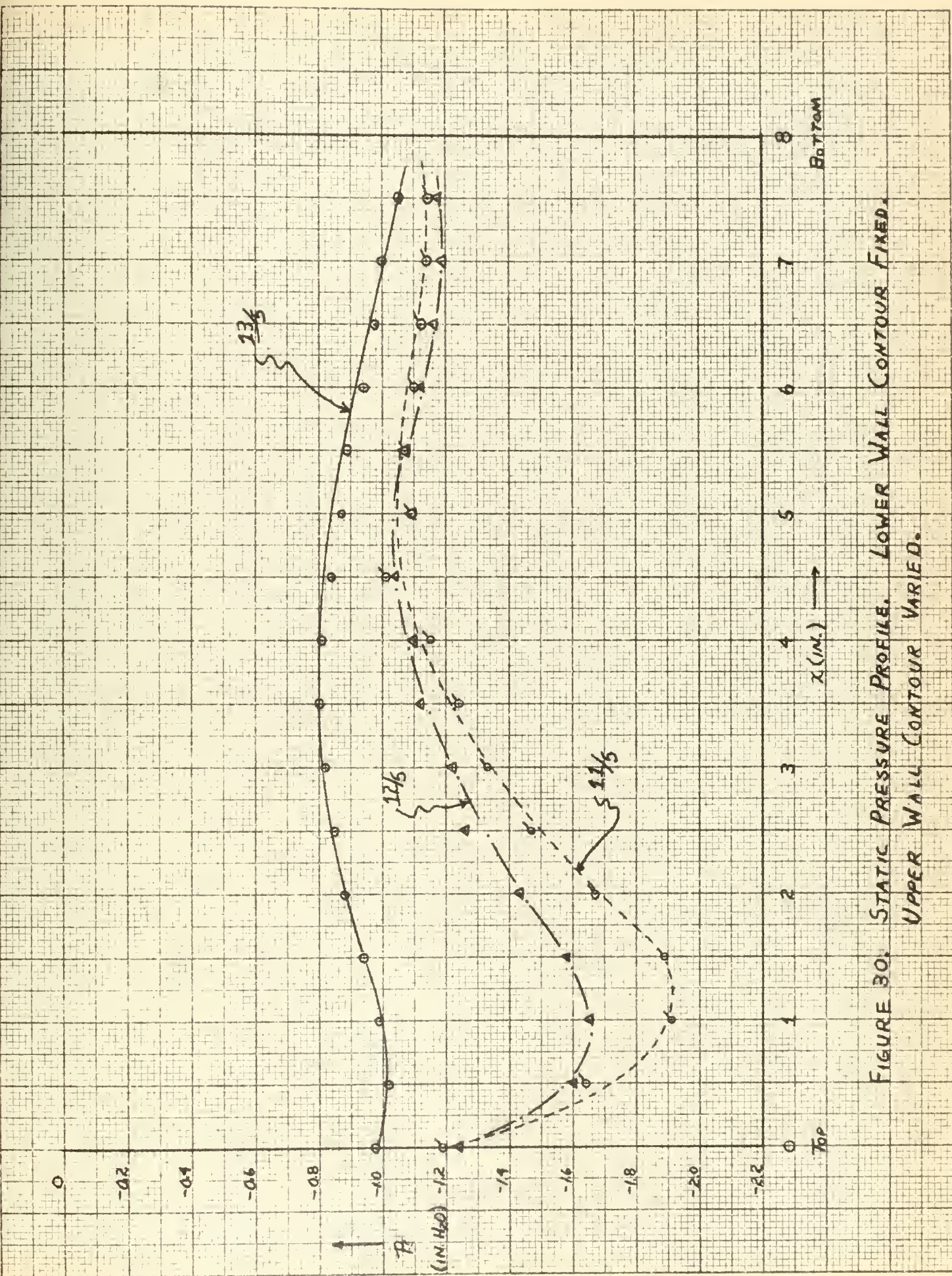


FIGURE 30. STATIC PRESSURE PROFILE. LOWER WALL CONTOUR FIXED. UPPER WALL CONTOUR VARIED.

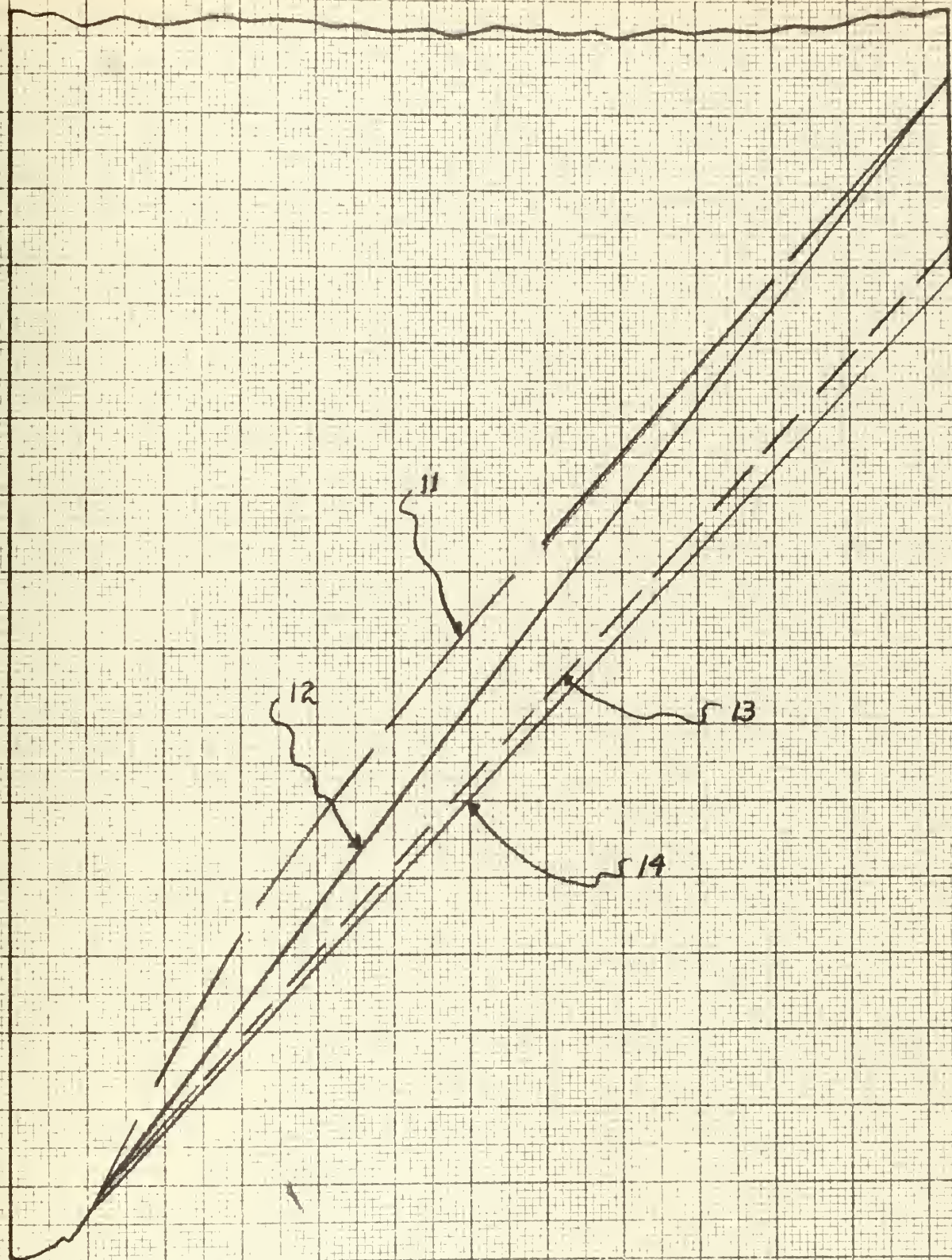


FIGURE 31 UPPER WALL CONTOURS. SCALE: FULL SIZE

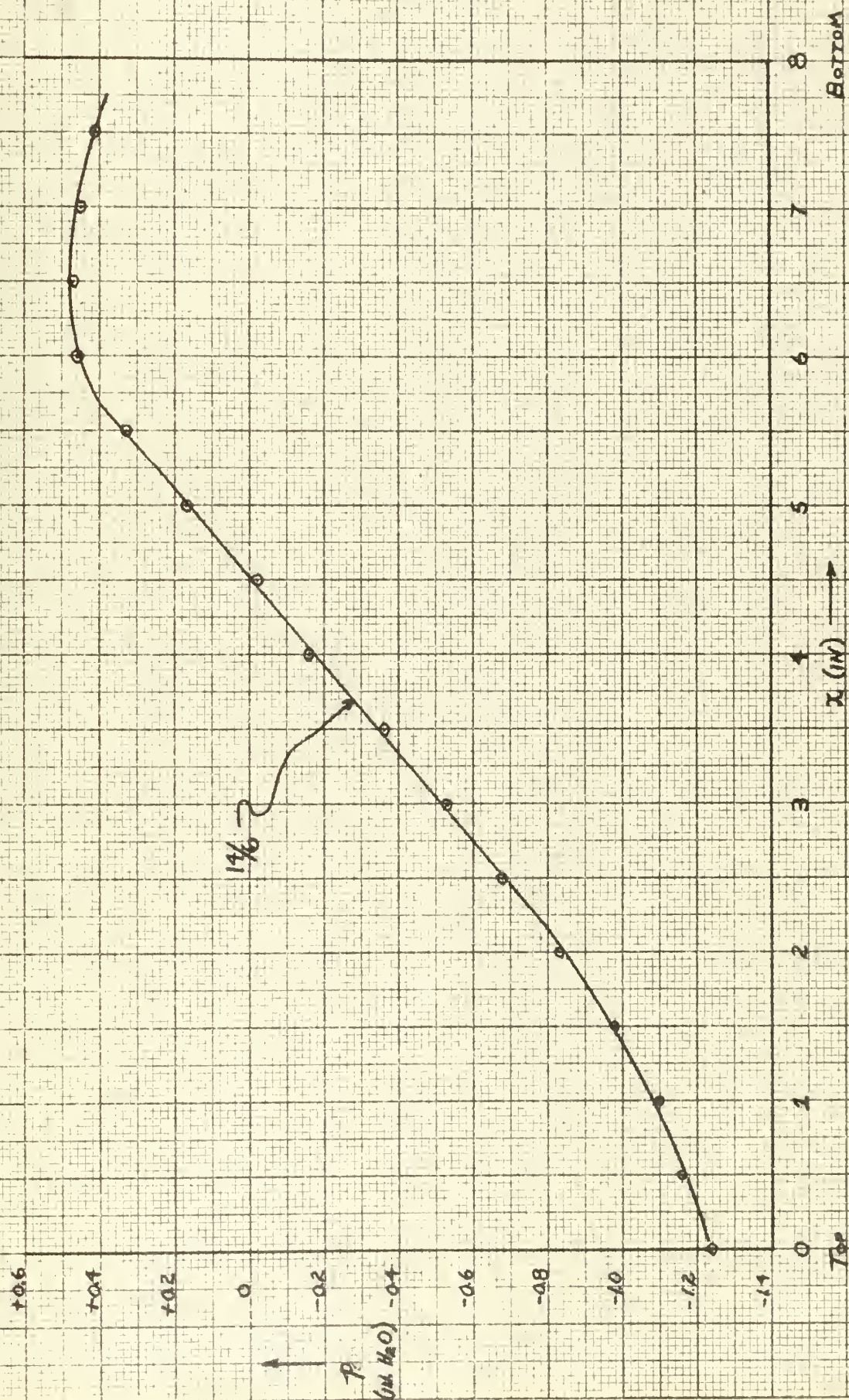


FIGURE 32. INITIAL STATIC PRESSURE PROFILE. TEST VANES REINSTALLED.

that the over-expansion of the fluid flow at the top of the cascade resulted in a decrease of static pressure, while the under-expansion of the fluid flow at the bottom of the cascade resulted in an increased static pressure. These effects were due to the action of the test vanes in turning the streamlines of the fluid flow downward as they passed around the test vanes. This condition was eliminated by notching away that portion of the upper and lower walls downstream of the mid-chord of the test vanes. In addition, the contour of the lower wall was adjusted in steps until it conformed with the shape of the streamlines of the fluid flow at the bottom of the cascade. Figure 33 shows the final static pressure profile. Figure 34 shows the various lower wall contours used before obtaining this profile.

With the wall configurations indicated in Fig. 33, the flow properties ahead of and after the cascade of test vanes were then determined. Figures 35, 36 and 37 show plots of representative values of total pressure P_t , static pressure P and flow angle α , respectively, measured ahead of the test vanes. Figures 38, 39 and 40 show plots of the same quantities measured after the test vanes.

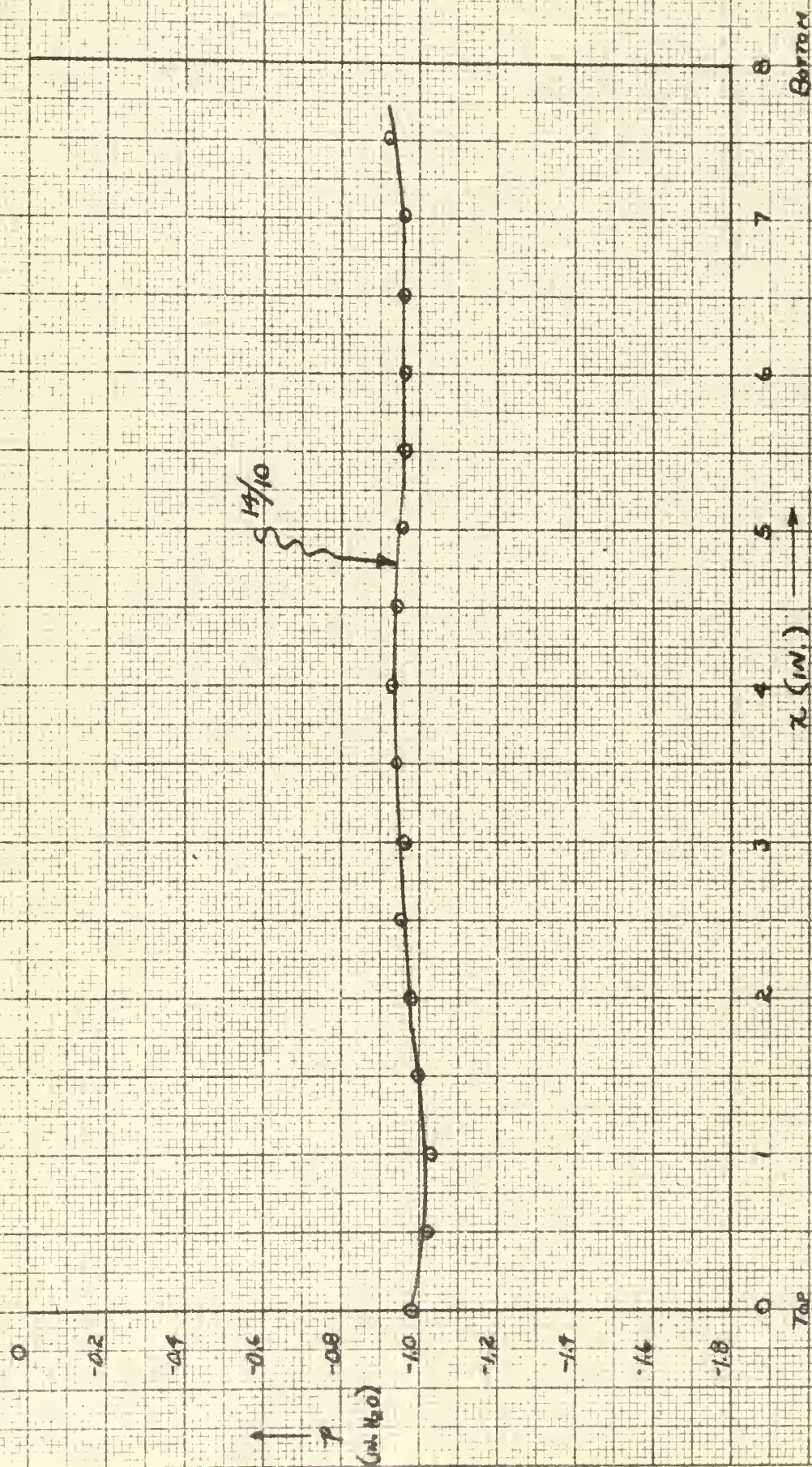


FIGURE 33 FINAL STATIC PRESSURE PROFILE. TEST VANES REINSTALLED.

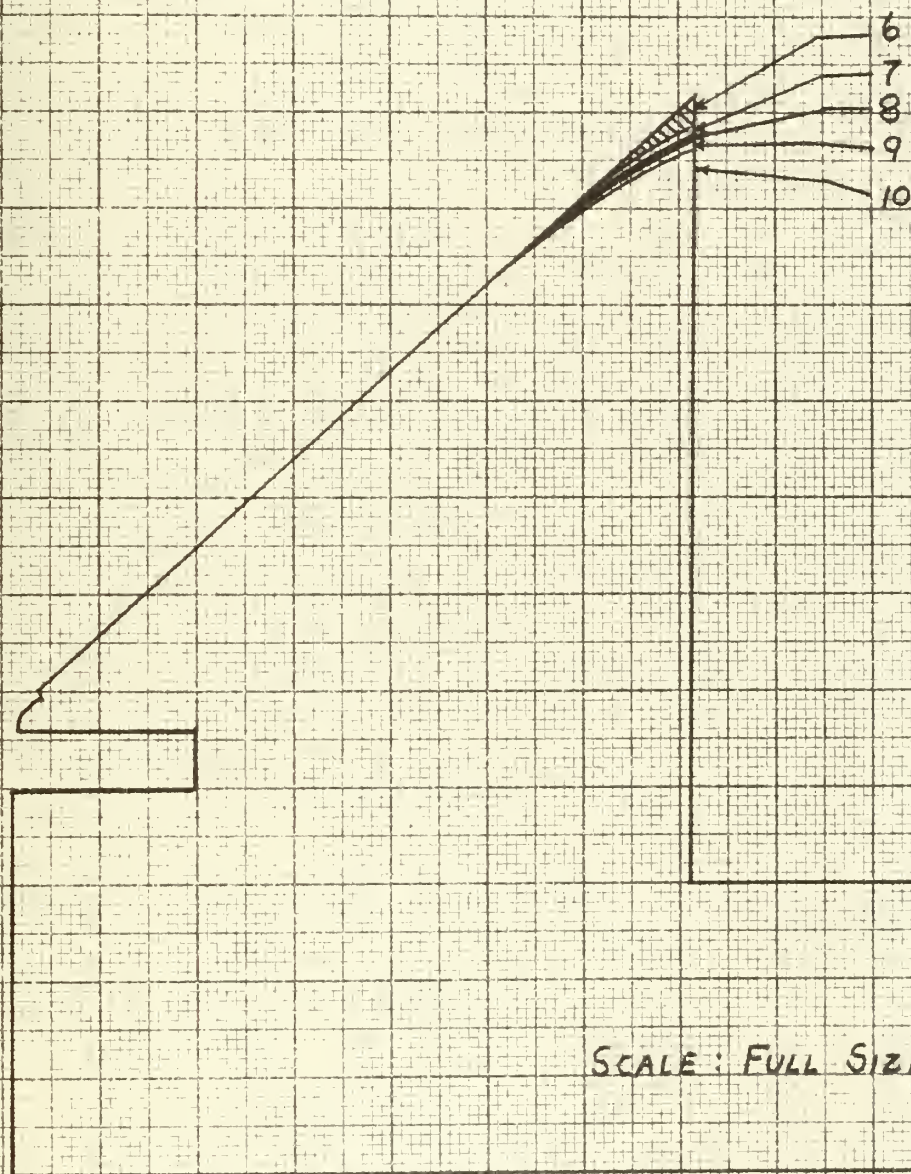


FIGURE 34. LOWER WALL CONTOURS WITH TEST VANES INSTALLED.

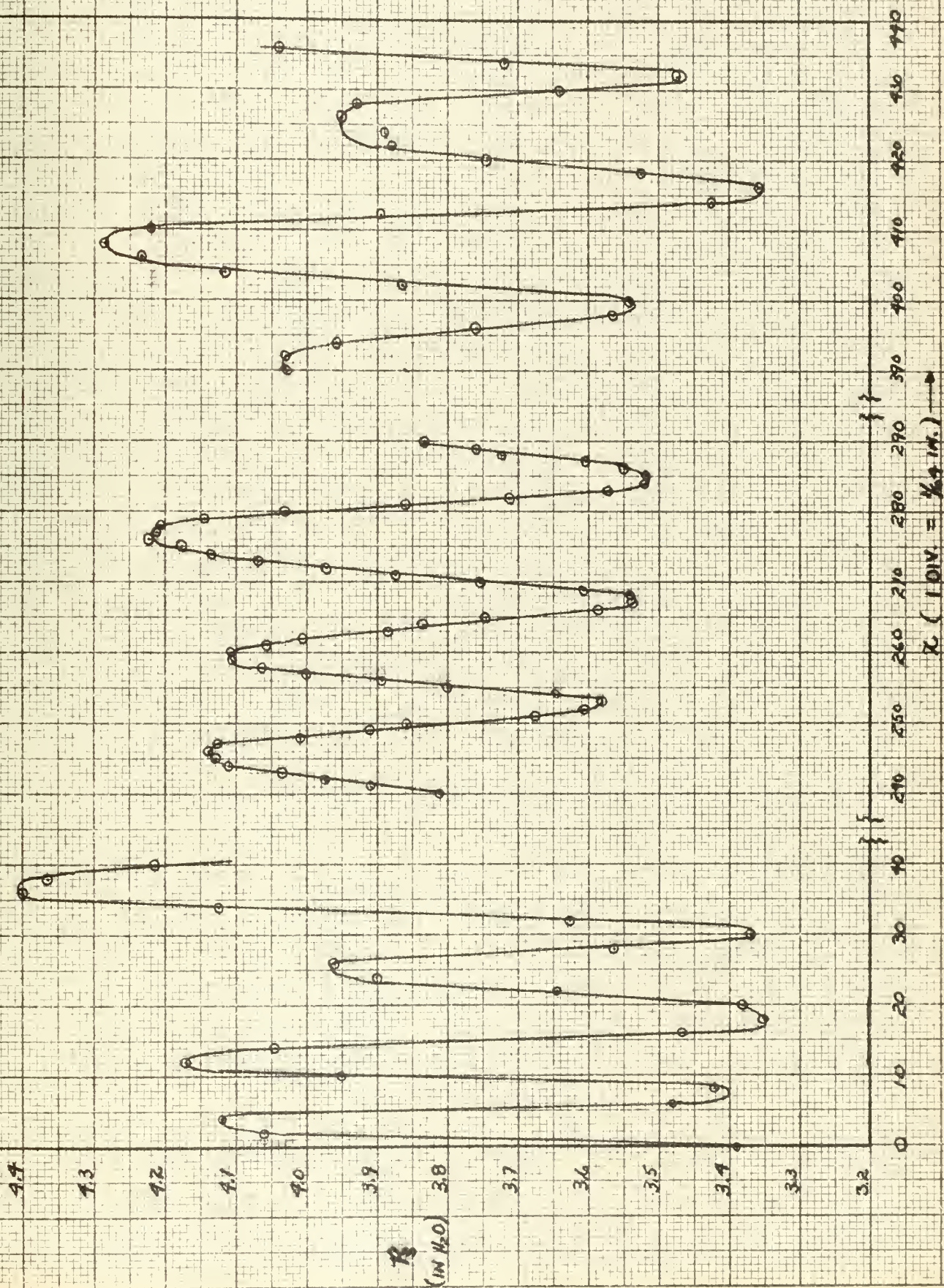


FIGURE 35. TOTAL PRESSURE AHEAD OF TEST VANES.

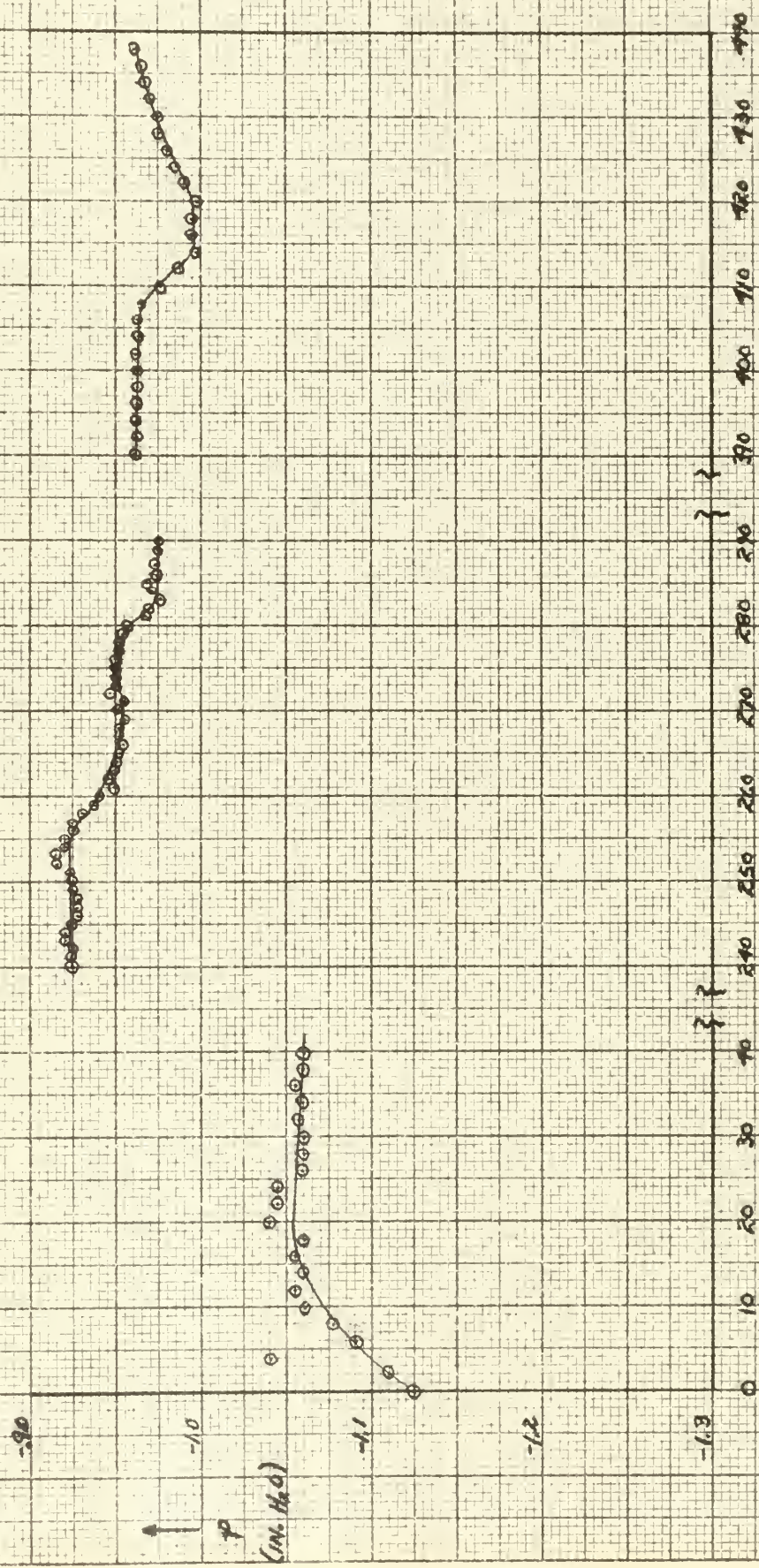


FIGURE 36. STATIC PRESSURE AHEAD OF TEST VANES.

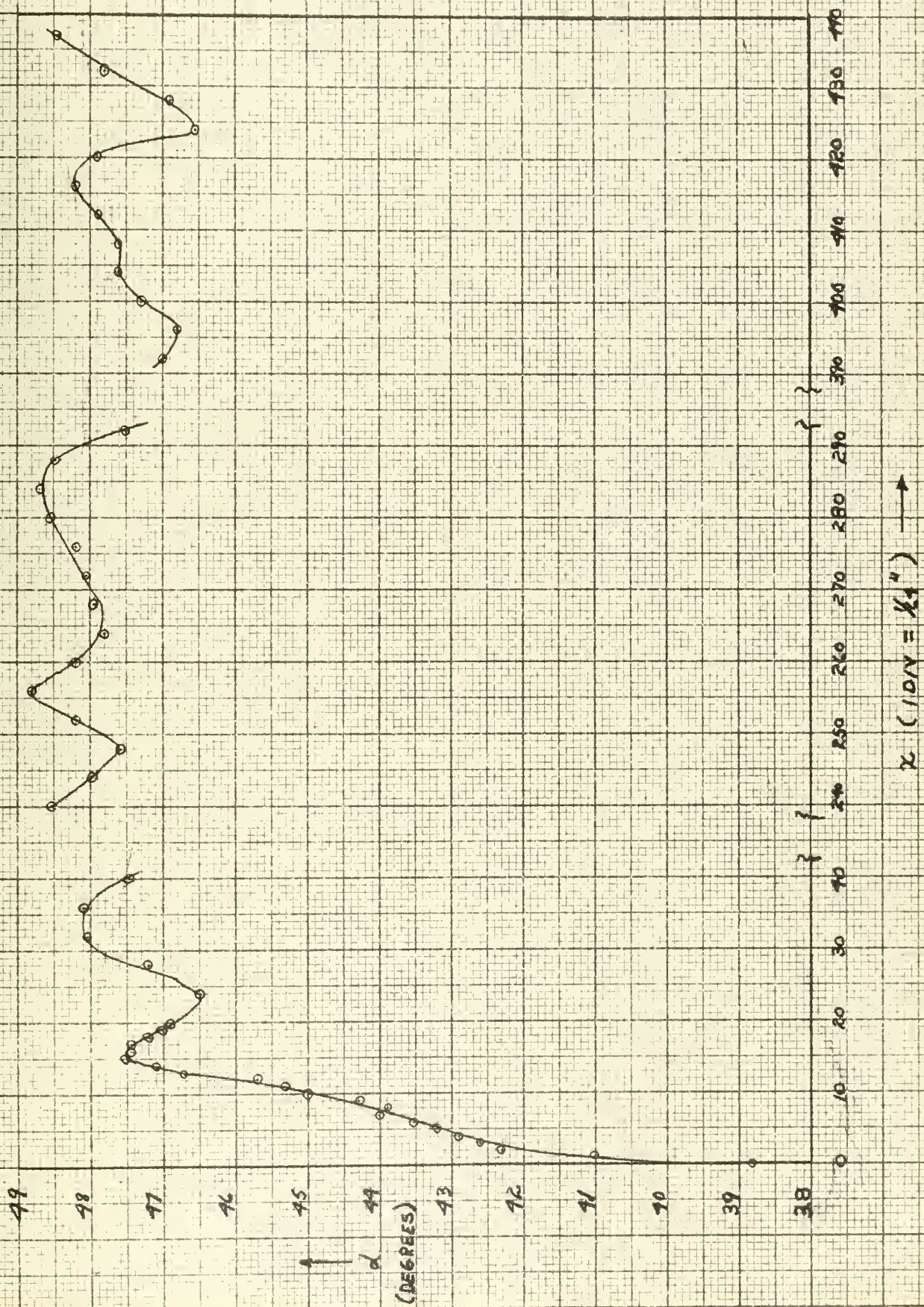
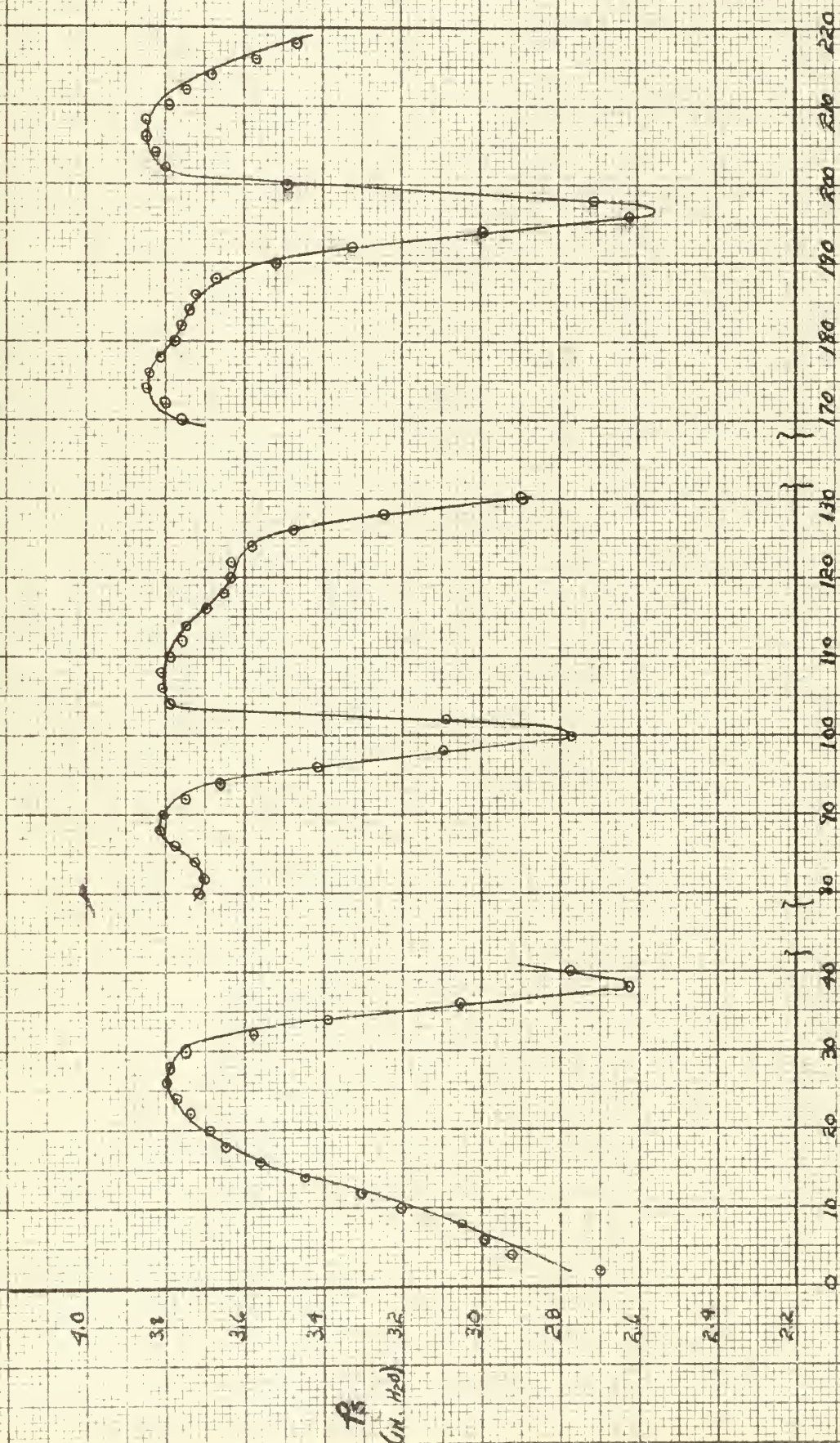
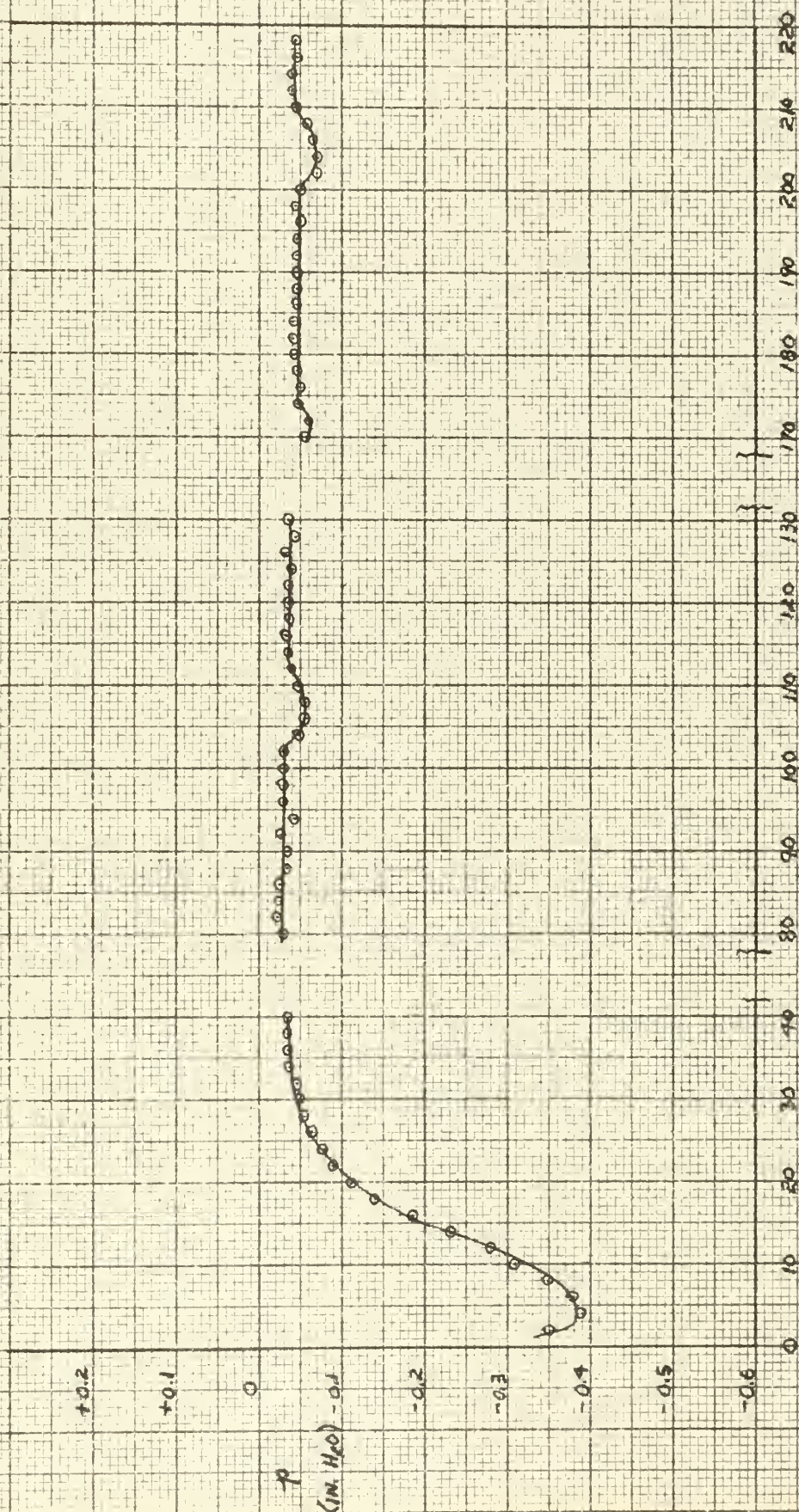


FIGURE 37. ANGLE OF FLUID FLOW AHEAD OF TEST VANES.



α (1 DIV = 7.32°)

FIGURE 38. TOTAL PRESSURE AFTER TEST VANES



x (1 DIV. = $\frac{1}{32}$ ")

FIGURE 39. STATIC PRESSURE AFTER TEST VANES.

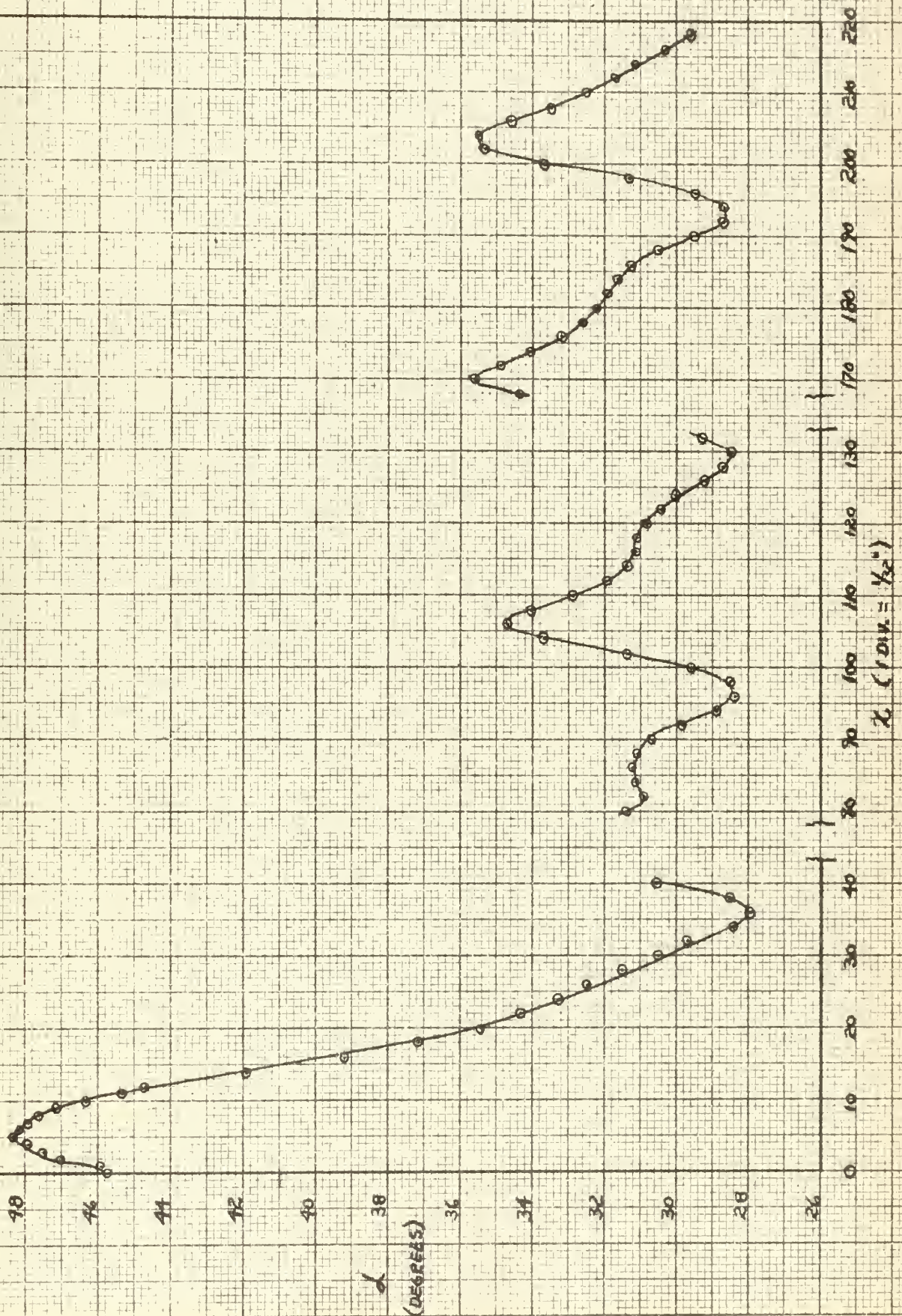


FIGURE 40. ANGLE OF FLUID FLOW AFTER TEST VANES.

9. Blade Loading Limit.

For a cascade having a fixed ratio of chord to span and the same fluid outlet angle, increasing the angle of incidence of the blades will increase the angle of deflection of the flow across the cascade. This is normally associated with an increase in the lift/drag ratio. However, if the angle of deflection exceeds certain limits, the lift drag ratio decreases. This stalling limit is of importance for the design since it establishes the permissible maximum loading of the blade. To estimate this loading limit, A.D.S. Carter³ has given an empirical relation which takes account of the blocking effect of blades of finite thickness.

$$2 \frac{A}{c} (\tan \beta_0 - \tan \beta_3) \frac{\cos^2 \beta_3}{\cos \beta_\infty} \times \frac{A/c}{A/c - \frac{2x}{c} \sec \beta_\infty} \leq \text{constant} \quad (87)$$

where x is the mean effective thickness of the blades.

The blades installed in the cascade had profiles with NACA 65-(15)10 section. They are NACA 65 Series airfoils with a design lift coefficient of 0.15 and a maximum thickness of ten per cent. The constant for zero blockage can be taken as 1.35. In addition, a value of $\frac{x}{c} \sec \beta_\infty$ of 1/12 is recommended by Carter for blades of ten per cent thickness. Substituting these values in Equation (87)

$$\frac{A}{c} (\tan \beta_0 - \tan \beta_3) \frac{\cos^2 \beta_3}{\cos \beta_\infty} \times \frac{6 A/c}{6 A/c - 1} \leq 0.675 \quad (88)$$

³A.D.S. Carter, Author of Chapter 5, Gas Turbine Principles and Practice, Sir Harold R. Cox, Editor, D. Van Nostrand Co., pp. 5-16---5-19, 1955.

With $\eta/c = 1/\sigma$, and multiplying by σ^2/σ , Equation (88) is

$$(\tan \beta_o - \tan \beta_3) \frac{\cos^2 \beta_3}{\cos \beta_o} \times \frac{b}{b-\sigma} \leq 0.675 \quad (89)$$

Multiplying by $\frac{b-\sigma}{b}$, there is

$$(\tan \beta_o - \tan \beta_3) \frac{\cos^2 \beta_3}{\cos \beta_o} \leq 0.1125 \sigma (b-\sigma) \quad (90)$$

For $\sigma=1$, the solidity of the cascade investigated, there is

$$(\tan \beta_o - \tan \beta_3) \frac{\cos^2 \beta_3}{\cos \beta_o} \leq 0.5625 \quad (91)$$

Evaluating the left hand side of Equation (91) using the values of β_o , β_3 and β_o determined from the test data, the values of the blade loading are 0.442 at one-quarter blade height, 0.468 at one-half blade height and 0.472 at three-quarters blade height. These values are less than the permissible maximum loading of 0.5625 specified by Carter.

10. Results.

The results calculated from the test data are shown in Table II. Table III contains a comparison of these results with those reported by Herrig, Emery and Erwin in NACA TN 3916⁴. Figure 31 of TN 3916 shows the turning angle $\Delta\beta$, drag coefficient C_D , lift coefficient C_L and the lift/drag ratio L/D plotted as a function of the angle of attack α_a for cascade solidity $\sigma = 1$. The angle between the inlet flow and the horizontal β_c was determined to be 47.7 degrees and in TN 3916 this angle was 45 degrees. The Reynolds number of the flow in the cascade was 72,000 compared to a Reynolds number of 245,000 for the flow in TN 3916. The lift coefficient calculated from the test data was 0.58 while in TN 3916 the lift coefficient was 0.845. The drag coefficient of the test vanes was 0.050 compared to a value of 0.014 in TN 3916. The value of the turning angle $\Delta\beta$ was evaluated to be 16.1 degrees whereas in TN 3916 the turning angle was found to be 29 degrees. Based upon the plots of drag coefficient and the lift/drag ratio as functions of the angle of attack, TN 3916 indicated a design angle of attack of 14.5 degrees. Lack of data for angles of attack other than 20.2 degrees precluded the prediction of a design angle of attack.

The large value of the evaluated drag coefficient may primarily be due to the lower Reynolds number of the flow in

⁴L. J. Herrig, J. C. Emery and J. R. Erwin, Systematic Two-Dimensional Cascade Tests of NACA 65-Series Compressor Blades at Low Speeds, NACA TN 3916, February 1957.

TABLE II
RESULTS CALCULATED FROM TEST DATA

Equation	Quantity	$h = \frac{1}{4}$	$h = \frac{1}{2}$	$h = \frac{3}{4}$	Units
28	V_{w_0}	98.5	98.1	98.4	Ft/sec
29	p_0	0.0333	0.0345	0.0348	#/in ²
30	V_{w_0}	106	109	110	ft/sec
31	β_0	47.0	47.7	48.2	deg.
32	V_0	145	148	148	ft/sec
33	V_{w_3}	106	108	107	ft/sec
34	p_3	0.00044	0.00109	0.00202	#/in ²
35	V_{w_3}	62.2	66.5	67.9	ft/sec
36	β_3	30.4	31.6	32.4	deg.
37	V_3	123	127	127	ft/sec
38	V_∞	132	135	135	ft/sec
38	V_{w_∞}	102	103	102	ft/sec
38	V_{w_0}	84.0	87.8	88.9	ft/sec
39	β_∞	39.4	40.5	40.9	deg.
22	F_w	0.0545	0.0619	0.0566	#
23	F_w	0.0914	0.0866	0.0875	#
20	F	0.106	0.106	0.104	#
21	ϕ	30.8	35.5	32.9	deg
40	D	0.016	0.0096	0.014	#
41	L	0.104	0.106	0.102	#
42	C_D	0.090	0.050	0.079	
43	C_L	0.59	0.58	0.56	
67	f	0.104	0.087	0.094	

TABLE II, Continued

Equation	Quantity	$h = \frac{1}{4}$	$h = \frac{1}{2}$	$h = \frac{3}{4}$	Units
79	C_o	0.078	0.065	0.068	
	$\Delta\beta$	16.6	16.1	15.8	deg
	$C_L\sigma$	0.59	0.58	0.56	
	M	0.117	0.120	0.120	
	N_R	70,300	72,000	72,000	
91	Blade Loading	0.442	0.468	0.472	

TABLE III
COMPARISON OF RESULTS

Quantity	Evaluated	TN 3916
α_w	20.2°	20.2°
β_o	47.7°	45°
σ	1.0	1.0
N_R	72,000	245,000
C_L	0.58	0.845
C_D	0.050	0.014
L/D	11.8	65
α_{DESIGN}		14.5
$\Delta \beta$	16.1°	29°

the cascade. For Reynolds numbers greater than 450,000 the profile drag of a cascade is almost constant and increases slightly as the Reynolds number decreases to about 150,000. The profile drag nearly doubles for decreases in Reynolds number from 150,000 to 75,000.

Figure 85(a) of TN 3916 shows that the effect of Reynolds number on the turning angle $\Delta\beta$ near the design angle of attack is almost insignificant for values of Reynolds number between 220,000 and 470,000. However, there is a decrease in the turning angle $\Delta\beta$ as the Reynolds number is decreased to a value of less than 220,000. The decrease in turning angle for flows of Reynolds number less than 220,000 was also reported by Rhoden⁵ in the results of an investigation of the effects of Reynolds number on test vanes of various camber angles. For a flow corresponding to the Reynolds number of this test Rhoden found $\Delta\beta$ to be 14.2 degrees for a test vane mean line camber angle of 20 degrees, 23.2 degrees for a mean line camber angle of 30 degrees and 28.1 degrees for a mean line camber angle of 40 degrees.

The design mean line camber angle for the test vanes used in this investigation, NACA 65-(15)10 section, is 33 degrees. Measurement of the mean line camber angle of the test vanes by means of an optical comparator showed this angle to be

⁵H. G. Rhoden, Effects of Reynolds Number on the Flow of Air through a Cascade of Compressor Blades, R & M No. 2919, June 1952.

30 degrees. In addition, the inlet and outlet angles of the test vanes were found to be smaller than those of the NACA 65-(15)10 section. The deviation of the test vane profile, particularly the lower surface of the trailing edge, causes some doubt as to the ability of the test vanes to cause flow deflections equal to those of the NACA 65-(15)10 section for flows of equal Reynolds number. It is considered that the smaller turning angle, and consequently the smaller coefficient of lift, calculated from the measured data is the result of the deviations of the test vane profile from the NACA 65-(15)10 section and the lower Reynolds number of the flow.

11. Conclusions.

It is the conclusion of the writer that an inlet guide vane assembly incorporated in the inlet of a cascade produces a nearly uniform static pressure profile from upper to lower wall and a regular distribution of fluid velocity and flow angle after the inlet guide vanes. Conditions of pressure, fluid velocity and flow angle were as found in conventional cascades. While the lift and drag coefficients and the turning angle do not compare favorably with those published for geometrically similar cascades without inlet guide vanes, it is thought that this was primarily the result of the lower Reynolds number used in this investigation, and the deviations of the test vanes from the NACA 65-(15)10 section.

Modifications suggested in the next section refer to methods of assisting the investigator in determining the static pressure profile and in increasing the accuracy of the angle measuring device and do not change the basic concept of the design.

12. Recommendations.

The installation of static pressure taps in the side walls of the cascade between the inlet guide vanes and the test vanes would facilitate the initial determination of the static pressure profile. With these static pressure taps spaced at intervals of, say, one inch, pressure leads from these static pressure taps could be connected to a manometer bank. This modification would give the investigator a visual picture of the static pressure profile. Such information would be helpful for the adjustment of the upper and lower wall contours of the cascade to obtain uniform pressure distributions. An indication of the static pressure profile across the width of the cascade could be obtained by placing pressure leads from oppositely located static pressure taps across a differential manometer.

It is further recommended that the method of upper and lower side wall construction be modified to permit adjustment of the upper and lower wall contours while the cascade is in operation. As shown in Fig. 41, such a modification would consist of pinning the upstream ends of the upper and lower walls as before, but would add a threaded screw arrangement to permit fine adjustment. Initial adjustment of the upper and lower walls would be made by rotating the entire wall assembly about the pinned joint.

Displacement of the upper and lower walls of the cascade by the movement of one of the threaded screws will tend

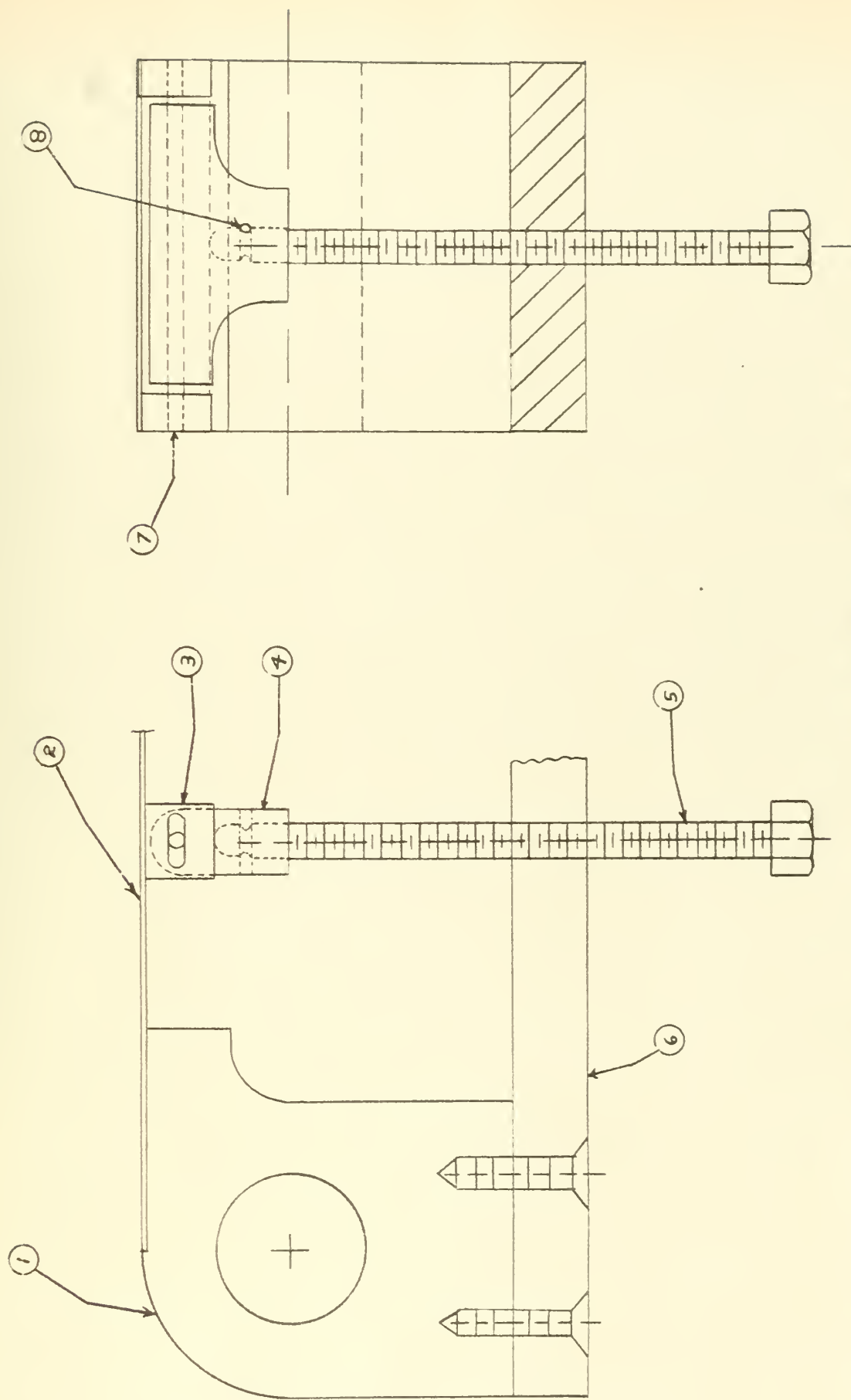


Figure 41. Upper And Lower Wall Modification Showing: 1- End Piece; 2- Wall; 3- Support Bracket; 4- Threaded Screw Holder; 5- Threaded Screw; 6- Bottom Piece; 7- Roller; 8- Pin.

to cause an axial rotation and a lateral displacement of adjacent support brackets. If the support brackets are rigidly fixed to the threaded screw such movement is not possible and an abrupt change in the slope of the wall will result at each support bracket. To eliminate this condition a channel must be provided in each support bracket. A roller inserted in the channel would pass through the threaded screw holder. The roller, being held in position by the threaded screw holder, would permit axial rotation and lateral displacement of the support bracket in response to the displacement of adjacent portions of the cascade wall.

Due to the large relative error in the present angle measuring device in comparison to that of the micromanometer it is recommended that it be increased in accuracy. This could be done by replacing the pointer arm-machinist rule method of measurement with an arrangement similar in operation to that of a marine sextant. The angle measuring probe would be mounted in the center of the device as before but the end of the scale arm would be machined in the arc of a circle and would be threaded to engage a vernier. The pin arrangement for pre-setting an angle into the device would be retained but a lever would be provided to disengage the vernier from the threads on the circumference of the scale arm to permit rapid initial adjustment.

BIBLIOGRAPHY

1. I. J. Herrig, J. C. Emery and J. R. Erwin, Systematic Two-Dimensional Cascade Tests of NACA 65-Series Compressor Blades at Low Speeds, NACA TN 3916, February, 1957.

APPENDIX

ACCURACY OF RESULTS

It is of interest to investigate the effect of the measuring devices on the accuracy of the results. The following rules and formulas are given by J. B. Scarborough.⁶

The error in a calculated result may be due to one or both of two sources: error in the data, and error in the calculations. The absolute error of a calculation is the numerical difference between the true value of a quantity and its approximate value as obtained by measurement or calculation. The relative error is the absolute error divided by the true value of the quantity and is the true index of the accuracy of a measurement or calculation.

To round off a number is to retain a certain number of digits, counted from the left, and to drop the others.

Numbers are rounded according to the following rule:

To round a number to m significant figures discard all digits to the right of the m th place. If the discarded number is less than half a unit in the m th place, leave the m th digit unchanged; if the discarded number is greater than half a unit in the m th place, add one to the m th digit. If the discarded number is exactly half a unit in the m th place, leave the m th digit unaltered if

⁶J. B. Scarborough, Numerical Mathematical Analysis, The Johns Hopkins Press, Chapter I, 1930.

it is an even number, but increase it by one if it is an odd number, in other words, round off so as to leave the m th digit an even digit in such cases.

When a number has been rounded off in accordance with the above rule, it is said to be correct to m significant figures.

For a function $N = f(w_1, w_2, w_3, \dots, w_n)$ (A-I-1) of several independent variables $w_1, w_2, w_3, \dots, w_n$ which are subject to the errors $\Delta w_1, \Delta w_2, \Delta w_3, \dots, \Delta w_n$, respectively, there will be an error ΔN in the function N , according to the relation

$$N + \Delta N = f(w_1 + \Delta w_1, w_2 + \Delta w_2, \dots, w_n + \Delta w_n) \quad (\text{A-I-2})$$

Expanding the right hand side of Equation (A-I-2) by Taylor's theorem for a function of several variables, and neglecting the squares, products and higher powers of the errors $\Delta w_1, \Delta w_2, \dots, \Delta w_n$, the error ΔN is

$$\Delta N = \frac{\partial N}{\partial w_1} \Delta w_1 + \frac{\partial N}{\partial w_2} \Delta w_2 + \dots + \frac{\partial N}{\partial w_n} \Delta w_n \quad (\text{A-I-3})$$

The right hand side of Equation (A-I-3) is the total Differential of the function N . For the relative error in N we have

$$E_r = \frac{\Delta N}{N} = \frac{\partial N}{\partial w_1} \frac{\Delta w_1}{N} + \frac{\partial N}{\partial w_2} \frac{\Delta w_2}{N} + \dots + \frac{\partial N}{\partial w_n} \frac{\Delta w_n}{N} \quad (\text{A-I-4})$$

Let N be a function of the form

$$N = \frac{K a^m b^n c^p}{d^q e^r} \quad (\text{A-I-5})$$

Then, using Equation (A-I-4), the relative error is

$$E_r = \frac{\Delta N}{N} = m \frac{\Delta a}{a} + n \frac{\Delta b}{b} + p \frac{\Delta c}{c} - q \frac{\Delta d}{d} - r \frac{\Delta e}{e} \quad (\text{A-I-6})$$

Since the errors $\Delta a \dots \Delta e$ are just as likely to be positive as negative, we must take all terms with the positive sign to be certain of the maximum error in N . The relative error is then

$$E_r \leq m \left| \frac{\Delta a}{a} \right| + n \left| \frac{\Delta b}{b} \right| + p \left| \frac{\Delta c}{c} \right| + q \left| \frac{\Delta d}{d} \right| + r \left| \frac{\Delta e}{e} \right| \quad (\text{A-I-7})$$

For the sum of m numbers each of which has been rounded off correctly to the same place, the error in the sum may be as great as $m/2$ units in the last significant figure. The average of ten or more numbers which are given to n significant figures is usually true to $n+1$ significant figures.

If k is the first significant figure of a number which is correct to n significant figures, and if the number contains more than one digit different from zero, then its p th power is correct to

$$n-1 \text{ significant figures if } p \leq k$$

$$n-2 \text{ significant figures if } p \leq 10k$$

and its r th root is correct to

$$n \text{ significant figures if } rk \geq 10$$

$$n-1 \text{ significant figures if } rk < 10$$

The data taken in this thesis consisted of values of static pressure p , total pressure p_s , and angle of fluid flow α , at stations 1 and 2. The values of static pressure and total pressure were read from micromanometers calibrated

to 0.001 inches. The indicating fluid was water. It is estimated that the error in reading the total pressure ΔP_s was ± 0.003 inches, and that Δp was ± 0.001 inches in reading the static pressure. Since the ratio of total pressure to static pressure was approximately four at station 1 and approximately 70 at station 2, the error in the static pressure was at least one order of magnitude smaller than the error in the total pressure. Therefore, the error in the static pressure will be ignored and the dynamic pressure P_0 , which is the algebraic difference of the total pressure and the static pressure, will be considered to have the same error as the total pressure. In measuring the angle of fluid flow α , the error in reading the machinists rule was ± 0.01 inches. The length of the pointer arm was seven inches. Thus the error in α , $\Delta \alpha$, was $0.01/7$, or 0.001428 radians.

With the conversion factor from inches of water to pounds per square foot, and substituting the numerical value of ρ , Equation (85) is

$$V_a^2 = 4467 (P_s - p) \cos^2 \alpha \quad (\text{A-I-8})$$

with $P_0 = P_s - p \quad (\text{A-I-9})$

Equation (A-I-8) is

$$V_a^2 = 4467 (P_0) \cos^2 \alpha \quad (\text{A-I-10})$$

With Equation (A-I-9), Equation (86) is

$$V_a V_w = 4467 (P_0) \cos \alpha \sin \alpha \quad (\text{A-I-11})$$

Data used in the calculations were values of V_a^2 , $V_a V_w$ and V_w based on measured values of P_0 and α at stations 1 and 2. Table IV shows representative values of

P_0 and α , together with the errors $\Delta\alpha$ and ΔP_0 , which will be used to determine the relative and absolute error in V_a^2 , $V_a V_w$ and V_a . The relative influence of the micromanometer error and the angle measuring device error will be shown.

TABLE IV
REPRESENTATIVE VALUES OF P_0 AND α

	Station 1	Station 2
P_0	4.843 mm H ₂ O	3.851 mm H ₂ O
α	47°21"	32°37"
$\Delta\alpha$	$\pm .001428$ rad.	$\pm .001428$ rad.
ΔP_0	$\pm .003$ mm H ₂ O	$\pm .003$ mm H ₂ O

Using Equations (A-I-7) and (A-I-11), the relative error in $V_a V_w$, at station 1 is

$$E_r \leq \left| \frac{\Delta K}{K} \right| + \left| \frac{\Delta P}{P} \right| + \left| \frac{\Delta \cos \alpha}{\cos \alpha} \right| + \left| \frac{\Delta \sin \alpha}{\sin \alpha} \right|$$

Using the values from Table IV, and with $\Delta \cos \alpha = -\sin \alpha \Delta \alpha$ and $\Delta \sin \alpha = \cos \alpha \Delta \alpha$, the relative error in $V_a V_w$, is

$$E_r \leq 0 + \frac{.003}{4.843} + .00143(1.086) + .00143 (.9212)$$

$$E_r \leq .00062 + .00287 = .00349$$

The absolute error is, for $V_a V_w = 10,780.2$, to six figures

$$E_a = (V_a V_w) E_r$$

$$E_a = 10,780.2(.00349)$$

$$E_a = 37.7, \text{ say } 40$$

Thus, the true value of V_{a_i}, V_{w_i} lies between 10,820.2 and 10,740.2. The best that can be done is to take the average of the two numbers and round off to three significant figures. Even then the result may be in error by one digit in the third place. It is observed from the above calculation that the angle measuring device error contributes approximately four times as much to the relative error than the micromanometer error.

Using Equations (A-I-7) and (A-I-10), the relative error in $V_{a_i}^2$ at station 1 is

$$E_r \leq \left| \frac{\Delta K}{K} \right| + \left| \frac{\Delta P_0}{P_0} \right| + 2 \left| \frac{\Delta \cos d}{\cos d} \right|$$

Using the values from Table IV, and with $\Delta \cos d = -\sin d \Delta d$, the relative error in $V_{a_i}^2$ is

$$E_r \leq 0 + \frac{.003}{4.843} + (.00143) (1.086)$$

$$E_r = .00062 + .00310 = .00372$$

The absolute error is, for $V_{a_i}^2 = 9930.20$ to six figures,

$$E_a = (V_{a_i}^2) E_r$$

$$E_a = 9930.20 (.00372)$$

$$E_a = 36.9, \text{ say } 40$$

The true value of $V_{a_i}^2$ lies between 9970.20 and 8890.20.

Taking the average of the two numbers and rounding off to two significant figures, the result may be in error by one digit in the second place. The error in the angle measuring device contributes approximately five times as much to

the relative error than the error in the micromanometer readings.

Following the rule given for the r th power of a number which is correct to n significant figures, the first significant figure being k , V_a will be correct to two significant figures as the product of $r.k > 10$.

Using Equations (A-I-7) and (A-I-11), the relative error in $V_{a_2} V_{w_2}$ at station 2 is

$$E_r = \left| \frac{\Delta K}{K} \right| + \left| \frac{\Delta P_0}{P_0} \right| + \left| \frac{\Delta \cos d}{\cos d} \right| + \left| \frac{\Delta \sin d}{\sin d} \right|$$

Then the relative error in $V_{a_2} V_{w_2}$ is

$$E_r \leq 0 + \frac{.003}{3.851} + .00143(.6399) + .00143(1.563)$$

$$E_r \leq .00078 + .00316 = .00394$$

For $V_{a_2} V_{w_2} = 7809.88$ to six figures, the absolute error is

$$E_a = (V_{a_2} V_{w_2}) E_r$$

$$E_a = 7809.88(.00394)$$

$$E_a = 30.8, \text{ say } 30$$

Thus, the true value of $V_{a_2} V_{w_2}$ lies between 7839.88 and 7779.88.

With the average of these values and rounding off to two significant figures, the result may be in error by one digit in the second place. Hence, the error in the angle measuring device contributes also approximately four times as much to the relative error as the error in the micromanometer.

Using Equations (A-I-7) and (A-I-10), the relative error in $V_{a_2}^2$ at station 2 is

$$E_r = \left| \frac{\Delta K}{K} \right| + \left| \frac{\Delta P_0}{P_0} \right| + 2 \left| \frac{\Delta \cos d}{\cos d} \right|$$

Thus, the relative error in $V_{a_2}^2$ is

$$E_r \leq 0 + \frac{.003}{3.851} + 2(.00143)(.7095)$$

$$E_r \leq .00078 + .00201 = .00279$$

The absolute error is, for $V_{a_2}^2 = 12,204.1$ to six figures

$$E_a = (V_{a_2}^2) E_r$$

$$E_a = 12,204.1(.00279)$$

$$E_a = 34.0, \text{ say } 35$$

Hence, the true value of $V_{a_2}^2$ lies between 12,239.4 and 12,169.4. Taking the average of the two numbers and rounding off to three significant figures, it is observed that the result may be in error by one digit in the third place. It may be seen that the error in the angle measuring device contributed approximately three times as much to the relative error as did the error in the micromanometer.

Following the rules given for the r th root of a number which is correct to m significant figures, the first significant figure being k , V_{a_2} will be correct to two significant figures as the product of $r.k < 10$.

From the preceding calculations we can draw the following conclusion:

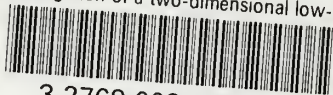
The average contribution to the relative error in the quantities $V_{a_2}^2$, $V_a V_w$ and V_w is approximately four times as great for the error in the angle measuring device as for the error in the micromanometer. The value of V_w will be correct to two significant figures. If the magnitude of $V_{a_2}^2$ or $V_w V_w$ is less than 10,000 it is correct to two significant figures;

if the magnitude of $V\omega^2$ or $V\omega V\omega$ is greater than 10,000 it is correct to three significant figures. In all cases the values of $V\omega^2$ and $V\omega V\omega$ may be in error by one digit in the last significant figure.

The calculated value of the drag and lift coefficients, C_D and C_L , respectively, are correct to two significant figures. The turning angle $\Delta\beta$ and the loss coefficient ξ are correct to three significant figures. All four of the above quantities may be in error by one digit in the last place.

thesE68

Investigation of a two-dimensional low-s



3 2768 002 06233 3

DUDLEY KNOX LIBRARY